Briefings in Bioinformatics, 2022, **23**, 1–31
https://doi.org/10.1093/bib/bbab531
Review

Deep learning tackles single-cell analysis—a survey of deep learning for scRNA-seq analysis

Mario Flores, Zhentao Liu, Tinghe Zhang, Md Musaddaqui Hasib, Yu-Chiao Chiu, Zhenqing Ye, Karla Paniagua, Sumin Jo, Jianqiu Zhang, Shou-Jiang Gao, Yu-Fang Jin, Yidong Chen and Yufei Huang

Corresponding authors: Mario Flores. E-mail: mario.flores@utsa.edu); Yidong Chen. E-mail: cheny8@uthscsa.edu; Yufei Huang. E-mail:yuh119@pitt.edu

Abstract

Since its selection as the method of the year in 2013, single-cell technologies have become mature enough to provide answers to complex research questions. With the growth of single-cell profiling technologies, there has also been a significant increase in data collected from single-cell profilings, resulting in computational challenges to process these massive and complicated datasets. To address these challenges, deep learning (DL) is positioned as a competitive alternative for single-cell analyses besides the traditional machine learning approaches. Here, we survey a total of 25 DL algorithms and their applicability for a specific step in the single cell RNA-seq processing pipeline. Specifically, we establish a unified mathematical representation of variational autoencoder, autoencoder, generative adversarial network and supervised DL models, compare the training strategies and loss functions for these models, and relate the loss functions of these models to specific objectives of the data processing step. Such a presentation will allow readers to choose suitable algorithms for their particular objective at each step in the pipeline. We envision that this survey will serve as an important information portal for learning the application of DL for scRNA-seq analysis and inspire innovative uses of DL to address a broader range of new challenges in emerging multi-omics and spatial single-cell sequencing.

Keywords: deep learning, single-cell RNA-seq, imputation, dimensionality reduction, clustering, batch correction, cell-type identificationfunctional prediction, visualization

Introduction

Single cell sequencing technology has been a rapidly developing area to study genomics, transcriptomics, proteomics, metabolomics and cellular interactions at the single cell level for cell-type identification, tissue composition and reprogramming [1, 2]. Specifically, sequencing of the transcriptome of single cells, or single-cell RNA-sequencing (scRNA-seq), has become the dominant technology in many frontier research areas such as disease progression and drug discovery [3, 4]. One

Mario Flores, PhD, is an Assistant Professor in the Department of Electrical and Computer Engineering at the University of Texas at San Antonio. His research focuses on DNA and RNA sequence methods, transcriptomics analysis (including scRNA-seq), epigenetics, comparative genomics and deep learning to study the mechanisms of gene regulation.
Zhentao Liu is a PhD student in the Department of Electrical and Computer Engineering, The University of Texas at San Antonio. His research focuses on deep learning for cancer genomics and drug response prediction.
Tinghe Zhang is a PhD student in the Department of Electrical and Computer Engineering, The University of Texas at San Antonio. His research focuses on deep learning for cancer genomics and drug response prediction.
Md Musaddaqui Hasib is a PhD student in the Department of Electrical and Computer Engineering, The University of Texas at San Antonio. His research focuses on interpretable deep learning for cancer genomics.
Yu-Chiao Chiu, PhD, is a Postdoctoral Fellow at the Greehey Children's Cancer Research Institute at The University of Texas Health San Antonio. His postdoctoral research is focused on developing deep learning models for pharmacogenomic studies.
Zhenqing Ye, PhD, is an Assistant Professor in the Department of Population Health Sciences and the bioinformatics facility manager at Greehey Children's Cancer Research Institute at The University of Texas Health San Antonio. His research focuses on computational methods on next-generation sequencing and single-cell RNA-seq data analysis.
Karla Paniagua is a PhD student in the Department of Electrical and Computer Engineering, The University of Texas at San Antonio. Her research focuses on applications of deep learning algorithms.
Sumin Jo is a PhD student in the Department of Electrical and Computer Engineering, The University of Texas at San Antonio. Her research focuses on m^{6}A mRNA methylation and deep learning for biomedical applications.
Jianqiu Zhang, PhD, is an Associate Professor in the Department of Electrical and Computer Engineering at the University of Texas at San Antonio. Her current research focuses on deep learning for biomedical applications such as m^{6}A mRNA methylation.
Shou-Jiang Gao, PhD, is a Professor in the UPMC Hillman Cancer Center and the Department of Microbiology and Molecular Genetics, University of Pittsburgh. His current research interests include Kaposi's sarcoma-associate herpesvirus, AIDS-related malignancies, translational and cancer therapeutics, and systems biology.
Yu-Fang Jin, PhD, is a Professor in the Department of Electrical and Computer Engineering at the University of Texas at San Antonio. Her research focuses on mathematical modeling of cellular responses in immune systems, data-driven modeling and analysis of macrophage activations, and deep learning applications.
Yidong Chen, PhD, is a Professor in the Department of Population Health Sciences and the director of Computational Biology and Bioinformatics at Greehey Children's Cancer Research Institute at the University of Texas Health San Antonio. His research interests include bioinformatics methods in next-generation sequencing technologies, integrative genomic data analysis, genetic data visualization and management, and machine learning in translational cancer research.
Yufei Huang, PhD, is a Professor in the Department of Medicine, University of Pittsburgh School of Medicine and Leader in AI Research at UPMC Hillman Cancer Center. His current research interests include uncovering the functions of m^{6}A mRNA methylation, cancer virology and medical AI & deep learning.

Received: September 16, 2021. **Revised:** November 15, 2021. **Accepted:** November 16, 2021

particular area where scRNA-seq has made a tangible impact is cancer, where scRNA-seq is becoming a powerful tool for understanding invasion, intratumor heterogeneity, metastasis, epigenetic alterations, detecting rare cancer stem cells and therapeutic response [5, 6]. Currently, scRNA-seq is applied to develop personalized therapeutic strategies that are potentially useful in cancer diagnosis, therapy resistance during cancer progression and the survival of patients [5, 7]. The scRNA-seq has also been adopted to combat COVID-19 to elucidate how the innate and adaptive host immune system miscommunicates, worsening the immunopathology produced during the viral infection [8, 9].

These studies have led to a massive amount of scRNA-seq data deposited to public databases such as the 10× single-cell gene expression dataset, Human Cell Atlas and Mouse Cell Atlas. Expressions of millions of cells from 18 species have been collected and deposited, waiting for further analysis (Single Cell Expression Atlas, EMBL-EBI, October 2021). On the other hand, due to biological and technical factors, scRNA-seq data present several analytical challenges related to its complex characteristics such as missing expression values, high technical and biological variance, noise and sparse gene coverage, and elusive cell identities [1]. These characteristics make it difficult to directly apply commonly used bulk RNA-seq data analysis techniques and have called for novel statistical approaches for scRNA-seq data cleaning and computational algorithms for data analysis and interpretation. To this end, specialized scRNA-seq analysis pipelines such as Seurat [10] and Scanpy [11], along with a large collection of task-specific tools, have been developed to address the intricate technical and biological complexity of scRNA-seq data.

Recently, deep learning (DL) has demonstrated its significant advantages in natural language processing and speech and facial recognition with massive data [12–14]. Such advantages have initiated the application of DL in scRNA-seq data analysis as a competitive alternative to conventional machine learning (ML) approaches for uncovering cell clustering [15, 16], cell-type identification [15, 17], gene imputation [18–20] and batch correction [21] in scRNA-seq analysis. Compared with conventional ML approaches, DL is more powerful in capturing complex features of high-dimensional scRNA-seq data. It is also more versatile, where a single model can be trained to address multiple tasks or adapted and transferred to different tasks. Moreover, DL training scales more favorably with the number of cells in scRNA-seq data size, making it particularly attractive for handling the ever-increasing volume of single cell data. Indeed, the growing body of DL-based tools has demonstrated DL's exciting potential as a learning paradigm to significantly advance the tools we use to interrogate scRNA-seq data.

In this paper, we present a comprehensive review of the recent advances of DL methods for solving the challenges in scRNA-seq data analysis (Table 1) from the quality control (QC), normalization/batch effect correction, dimensionality reduction, visualization, feature selection and data interpretation by surveying DL papers published up to April 2021. In order to maintain high quality for this review, we choose not to include any (bio)archival papers, although a proportion of these manuscripts contain important new findings that would be published after completing their peer-reviewed process. Previous efforts to review the recent advances in ML methods focused on efficient integration of single cell data [22, 23]. A recent review of DL applications on single cell data has summarized 21 DL algorithms that might be deployed in single cell studies [24]. It also evaluated the clustering and data correction effect of these DL algorithms using 11 datasets.

In this review, we focus more on the DL algorithms with a much detailed explanation and comparison. Furthermore, to better understand the relationship of each surveyed DL model with the overall scRNA-seq analysis pipeline, we organize the surveys according to the challenge they address and discuss these DL models following the analysis pipeline. A unified mathematical description of the surveyed DL models is presented and the specific model features are discussed when reviewing each method. This will also shed light on the modeling connections among the surveyed DL methods and the recognization of the uniqueness of each model. Besides the models, we also summarize the evaluation matrics used by these DL algorithms and methods that each DL algorithm was compared with. The online location of the code, the development platform and the used datasets for each method are also cataloged to facilitate their utilization and additional effort to improve them. Finally, we also created a companion online version of the paper at https://huang-ai4medicine-lab.github.io/survey-of-DL-for-scRNA-seq-analysis/_book/, which includes expanded discussion as well as a survey of additional methods. We envision that this survey will serve as an important information portal for learning the application of DL for scRNA-seq analysis and inspire innovative use of DL to address a broader range of new challenges in emerging multi-omics and spatial single-cell sequencing.

Overview of the scRNA-seq processing pipeline

Various scRNA-seq techniques (such as SMART-seq, Drop-seq and 10× genomics sequencing) [25, 26] are available nowadays with their sets of advantages and disadvantages. Despite the differences in the scRNA-seq techniques, the data content and processing steps of scRNA-seq data are quite standard and conventional. A typical scRNA-seq dataset consists of three files: genes quantified (gene IDs), cells quantified (cellular barcode) and a count matrix (number of cells × number of genes), irrespective of the technology or pipeline used. A series of essential steps in the scRNA-seq data processing pipeline and optional tools for each step with both ML and DL approaches are illustrated in Figure 1.

With the advantage of identifying each cell and unique molecular identifiers (UMIs) for expressions of each gene

Table 1. DL algorithms reviewed in the paper

App	Algorithm	Models	Evaluation	Environment	Codes	Refs
Imputation						
	DCA	AE	DREMI	Keras, Tensorflow, scanpy	https://github.com/theislab/dca	[18]
	SAVER-X	AE + TL	t-SNE, ARI	R/sctransfer	https://github.com/jingshuw/SAVERX	[58]
	DeepImpute	DNN	MSE, Pearson's correlation	Keras/Tensorflow	https://github.com/lanagarmire/DeepImpute	[20]
	LATE	AE	MSE	Tensorflow	https://github.com/audreyqyfu/LATE	[59]
	scGAMI	AE	NMI, ARI, HS and CS	Tensorflow	https://github.com/QUST-AIBBDRC/scGMAI/	[60]
	scIGANs	GAN	ARI, ACC, AUC and F-score	PyTorch	https://github.com/xuyungang/scIGANs	[19]
Batch correction						
	BERMUDA	AE + TL	KNN batch-effect test (kBET), the entropy of Mixing, SI	PyTorch	https://github.com/txWang/BERMUDA	[63]
	DESC	AE	ARI, KL	Tensorflow	https://github.com/eleozzr/desc	[67]
	iMAP	AE + GAN	kBET, Local Inverse Simpson's Index (LISI)	PyTorch	https://github.com/Svvord/iMAP	[70]
Clustering, latent representation, dimension reduction and data augmentation						
	Dhaka	VAE	ARI, Spearman Correlation	Keras/Tensorflow	https://github.com/MicrosoftGenomics/Dhaka	[72]
	scvis	VAE	KNN preservation, log-likelihood	Tensorflow	https://bitbucket.org/jerry00/scvis-dev/src/master/	[75]
	scVAE	VAE	ARI	Tensorflow	https://github.com/scvae/scvae	[76]
	VASC	VAE	NMI, ARI, HS and CS	H5py, keras	https://github.com/wang-research/VASC	[77]
	scDeepCluster	AE	ARI, NMI, clustering accuracy	Keras, Scanpy	https://github.com/ttgump/scDeepCluster	[79]
	cscGAN	GAN	t-SNE, marker genes, MMD, AUC	Scipy, Tensorflow	https://github.com/imsb-uke/scGAN	[82]
Multi-functional models (IM: imputation, BC: batch correction, CL: clustering)						
	scVI	VAE	**IM**: L_1 distance; **CL**: ARI, NMI, SI**;** **BC**: Entropy of Mixing	PyTorch, Anndata	https://github.com/YosefLab/scvi-tools	[17]
	LDVAE	VAE	Reconstruction errors	Part of scVI	https://github.com/YosefLab/scvi-tools	[86]
	SAUCIE	AE	**IM**: R^2 statistics; **CL**: SI**;** **BC**: modified kBET; Visualization: Precision/Recall	Tensorflow	https://github.com/KrishnaswamyLab/SAUCIE/	[15]
	scScope	AE	**IM**:Reconstruction errors**;** **BC**: Entropy of mixing**;** **CL**: ARI	Tensorflow, Scikit-learn	https://github.com/AltschulerWu-Lab/scScope	[92]
Cell-type Identification						
	DigitalDLSorter	DNN	Pearson correlation	R/Python/Keras	https://github.com/cartof/digitalDLSorter	[51]
	scCapsNet	CapsNet	Cell-type Prediction accuracy	Keras, Tensorflow	https://github.com/wanglf19/scCaps	[52]
	netAE	VAE	Cell-type Prediction accuracy, t-SNE for visualization	pyTorch	https://github.com/LeoZDong/netAE	[101]
	scDGN	DANN	Prediciton accuracy	pyTorch	https://github.com/SongweiGe/scDGN	[53]
Function analysis						
	CNNC	CNN	AUROC, AUPRC and accuracy	Keras, Tensorflow	https://github.com/xiaoyeye/CNNC	[54]
	scGen	VAE	Correlation, visualization	Tensorflow	https://github.com/theislab/scgen	[114]

DL Model keywords: AE + TL: autoencoder with transfer learning, DANN: domain adversarial neural network, CapsNet: capsule neural network

in a single cell, scRNA-seq data are embedded with increased technical noise and biases [27]. QC is the first and the key step to filter out dead cells, double-cells or cells with failed chemistry or other technical artifacts. The most commonly adopted three QC covariates include the number of counts (count depth) per barcode

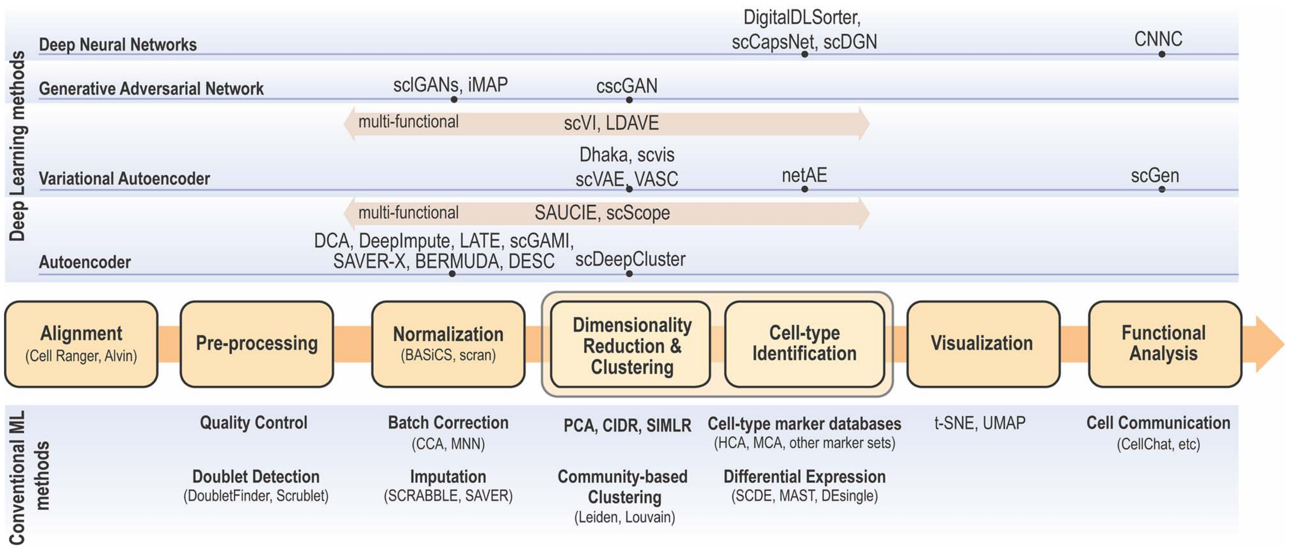
Deep Learning methods
Deep Neural Networks
DigitalDLSorter, scCapsNet, scDGN
CNNC
Generative Adversarial Network
scIGANs, iMAP
cscGAN
multi-functional
scVI, LDAVE
Variational Autoencoder
Dhaka, scvis scVAE, VASC
netAE
scGen
multi-functional
SAUCIE, scScope
Autoencoder
DCA, DeepImpute, LATE, scGAMI, SAVER-X, BERMUDA, DESC
scDeepCluster
Alignment (Cell Ranger, Alvin)
Pre-processing
Normalization (BASiCS, scran)
Dimensionality Reduction & Clustering
Cell-type Identification
Visualization
Functional Analysis
Conventional ML methods
Quality Control
Doublet Detection (DoubletFinder, Scrublet)
Batch Correction (CCA, MNN)
Imputation (SCRABBLE, SAVER)
PCA, CIDR, SIMLR
Community-based Clustering (Leiden, Louvain)
Cell-type marker databases (HCA, MCA, other marker sets)
Differential Expression (SCDE, MAST, DEsingle)
t-SNE, UMAP
Cell Communication (CellChat, etc)

Figure 1. Single cell data analysis steps for both conventional ML methods (bottom) and DL methods (top). Depending on the input data and analysis objectives, major scRNA-seq analysis steps are illustrated in the center flow chart (color boxes) with conventional ML approaches along with optional analysis modules below each analysis step. DL approaches are categorized as DNN, GAN, VAE, and AE. For each DL approach, optional algorithms are listed on top of each step.

identifying each cell, the number of genes per barcode and the fraction of counts from mitochondrial genes per barcode [28].

Normalization is designed to eliminate imbalanced sampling, cell differentiation, viability and many other factors. Approaches tailored for scRNA-seq have been developed including the Bayesian-based method coupled with spike-in, or BASiCS [29], deconvolution approach, scran [30] and scTransfrom in Seurat where regularized Negative Binomial Regression was proposed [31]. Two important steps, batch correction and imputation, will be carried out if required by the analysis.

- **Batch Correction** is a common source of technical variation in high-throughput sequencing experiments due to variant experimental conditions such as technicians and experimental time, imposing a major challenge in scRNA-seq data analysis. Batch effect correction algorithms include detection of mutual nearest neighbors (MNNs) [32], canonical correlation analysis (CCA) with Seurat [33] and Harmony algorithm through cell-type representation [34].
- **Imputation** step is necessary to handle high sparsity data matrix, due to missing value or dropout in scRNA-seq data analysis. Several tools have been developed to 'impute' zero values in scRNA-seq data, such as SCRABBLE [35], SAVER [36] and scImpute [37].

Dimensionality reduction and visualization are essential steps to represent biologically meaningful variations and high dimensionality with significantly reduced computational cost. Dimensionality reduction methods, such as principal component analysis (PCA), are widely used in scRNA-seq data analysis to achieve that purpose. More advanced nonlinear approaches that preserve the topological structure and avoid overcrowding in lower dimension representation, such as LLE [38] (used in SLICER [39]), *t*-SNE [40] and UMAP [41], have also been developed and adopted as a standard in single-cell data visualization.

Clustering analysis is a key step to identify cell subpopulations or distinct cell types to unravel the extent of heterogeneity and their associated cell-type-specific markers. Unsupervised clustering is frequently used to categorize cells into clusters according to their similarity often measured in the aforementioned dimensionality-reduced representations. Some of popular algorithms include the community detection algorithm Louvain [42] and Leiden [43], and data-driven dimensionality reduction followed with k-Means cluster by SIMLR [44].

Feature selection is another important step in single-cell RNA-seq analysis to select a subset of genes, or features, for cell-type identification and functional enrichment of each cluster. This step is achieved by differential expression analysis designed for scRNA-seq, such as MAST that used linear model fitting and likelihood ratio testing [45]; SCDE that adopted a Bayesian approach with a Negative Binomial model for gene expression and Poisson process for dropouts [46], or DEsingle that utilized a Zero-Inflated Negative Binomial (ZINB) model to estimate the dropouts [47].

Besides these key steps, downstream analyses include cell-type identification, coexpression analysis, prediction of perturbation response, where DL has also been applied. Other advanced analyses including trajectory inference and velocity and pseudotime analysis are not discussed here because most of the approaches on these topics are non-DL based.

Overview of common DL models for scRNA-seq analysis

We start our review by introducing the general formulations of widely used DL models. As most of the tasks including batch correction, dimensionality reduction, imputation and clustering are unsupervised learning tasks, we will give special attention to unsupervised models including variational autoencoder (VAE), the autoencoder (AE) or generative adversarial networks (GAN). We will also discuss the general supervised and transfer learning formulations, which find their applications in cell-type predictions and functional studies. We will discuss these models in the context of scRNA-seq, detailing the different features and training strategies of each model and bringing attention to their uniqueness.

Variational autoencoder

Let $\mathbf{x}_n$ represent a $G \times 1$ vector of expression levels (UMI counts or normalized, log-transformed expression) of G genes in cell n, where $p(x_{gn}|\ \nu_{gn}, \alpha_{gn})$ follows some distribution(e.g. ZINB or Gaussian), where $\nu_{gn}$and α_{gn} are distribution parameters (e.g. mean, variance or dispersion) (Figure 2A). We consider ν_{gn} to be of particular interest (e.g. the mean counts) and is thus further modeled by a decoder neural network $D_{\boldsymbol{\theta}}$ (Figure 2A) as

$$\boldsymbol{\nu}_n = D_{\boldsymbol{\theta}}\left(\mathbf{z}_n, s_n\right), \tag{1}$$

where the gth element of $\boldsymbol{\nu}_n$ is ν_{gn} and $\boldsymbol{\theta}$ is a vector of decoder weights, $\mathbf{z}_n \in \mathbb{R}^d$ represents a latent representation of gene expression and is used for visualization and clustering and s_n is an observed variable (e.g. the batch ID). For VAE, $\mathbf{z}_n$ is commonly assumed to follow a multivariate standard Normal prior, i.e. $p(\mathbf{z}_n) = \mathcal{N}(0, \mathbf{I}_d)$ with $\mathbf{I}_d$ being a $d \times d$ identity matrix. Furthermore, α_{gn} of $p(x_{gn}|\ \nu_{gn}, \alpha_{gn})$ is a nuisance parameter, which has a prior distribution $p(\alpha_{gn})$ and can be either estimated or marginalized in variational inference. Now define $\boldsymbol{\Theta} = \{\boldsymbol{\theta}, \alpha_{ng} \forall n, g\}$. Then, $p(x_{gn}|\ \nu_{gn}, \alpha_{gn})$ and (1) together define the likelihood $p(\mathbf{x}_n|\mathbf{z}_n, s_n, \boldsymbol{\Theta})$.

The goal of training is to compute the maximum likelihood estimate of $\boldsymbol{\Theta}$

$$\begin{aligned}\hat{\boldsymbol{\Theta}}_{ML} &= \text{argmax}_{\boldsymbol{\Theta}} \sum\nolimits_{n=1}^{N} \log p\left(\mathbf{x}_n|s_n, \boldsymbol{\Theta}\right) \\ &\approx \text{argmax}_{\boldsymbol{\Theta}} \sum\nolimits_{n=1}^{N} \mathcal{L}\left(\boldsymbol{\Theta}\right),\end{aligned} \tag{2}$$

where $\mathcal{L}(\boldsymbol{\Theta})$ is the evidence lower bound (ELBO)

$$\begin{aligned}\mathcal{L}\left(\boldsymbol{\Theta}\right) &= \mathrm{E}_{q(\mathbf{z}_n|\mathbf{x}_n, s_n, \boldsymbol{\Theta})}\left[\log p\left(\mathbf{x}_n|\mathbf{z}_n, s_n, \boldsymbol{\Theta}\right)\right] \\ &\quad - D_{KL}\left[q\left(\mathbf{z}_n|\mathbf{x}_n, s_n, \boldsymbol{\Theta}\right) \| p\left(\mathbf{z}_n\right)\right],\end{aligned} \tag{3}$$

and $q(\mathbf{z}_n|\mathbf{x}_n, s_n)$ is an approximate to $p(\mathbf{z}_n|\mathbf{x}_n, s_n)$ and assumed as

$$q\left(\mathbf{z}_n|\mathbf{x}_n, s_n\right) = \mathcal{N}\left(\boldsymbol{\mu}_{zn}, diag\left(\boldsymbol{\sigma}^2_{Zn}\right)\right), \tag{4}$$

with $\{\boldsymbol{\mu}_{zn}, \boldsymbol{\sigma}^2_{Zn}\}$ given by an encoder network $E_{\boldsymbol{\phi}}$ (Figure 2A) as

$$\left\{\boldsymbol{\mu}_{zn}, \boldsymbol{\sigma}^2_{Zn}\right\} = E_{\boldsymbol{\phi}}\left(\mathbf{x}_n, s_n\right), \tag{5}$$

where $\boldsymbol{\phi}$is the weights vector. Now, $\boldsymbol{\Theta} = \{\boldsymbol{\theta}, \boldsymbol{\phi}, \alpha_{ng} \forall n, g\}$ and Eq. (2) is solved by the stochastic gradient descent approach while a model is trained.

All the surveyed papers that deploy VAE follow this general modeling process. However, a more general formulation has a loss function defined as

$$L\left(\boldsymbol{\Theta}\right) = -\mathcal{L}\left(\boldsymbol{\Theta}\right) + \sum\nolimits_{k=1}^{K} \lambda_k L_k\left(\boldsymbol{\Theta}\right), \tag{6}$$

where $L_k \forall k = 1, \ldots, K$ are losses for different functions (clustering, cell-type prediction, etc.) and λ_ks are the Lagrange multipliers. With this general formulation, for each paper, we examined the specific choices of data distribution $p(x_{gn}|\ \nu_{gn}, \alpha_{gn})$ that define $\mathcal{L}(\boldsymbol{\Theta})$, different L_k designed for specific functions, and how the decoder and encoder were applied to model different aspects of scRNA-seq data.

Autoencoders

AEs learn the low dimensional latent representation $\mathbf{z}_n \in \mathbb{R}^d$ of expression $\mathbf{x}_n$. The AE includes an encoder $E_{\boldsymbol{\phi}}$ and a decoder $D_{\boldsymbol{\theta}}$ (Figure 2B) such that

$$\mathbf{z}_n = E_{\boldsymbol{\phi}}\left(\mathbf{x}_n\right); \hat{\mathbf{x}}_n = D_{\boldsymbol{\theta}}\left(\mathbf{z}_n\right), \tag{7}$$

where $\boldsymbol{\Theta} = \{\boldsymbol{\theta}, \boldsymbol{\phi}\}$ are encoder and decoder weight parameters, respectively, and $\hat{\mathbf{x}}_n$ defines the parameters (e.g. mean) of the likelihood $p(\mathbf{x}_n|\boldsymbol{\Theta})$ (Figure 2B) and is often considered as imputed and denoised expressions. Additional design can be included in an AE model for batch correction, clustering and other objectives.

The training of an AE model is generally carried out by stochastic gradient descent algorithms to minimize the loss similar to Eq. (6) except $\mathcal{L}(\boldsymbol{\Theta}) = -\log p(\mathbf{x}_n|\boldsymbol{\Theta})$. When $p(\mathbf{x}_n|\boldsymbol{\Theta})$ is the Gaussian, $\mathcal{L}(\boldsymbol{\Theta})$ becomes the mean square error (MSE) loss

$$\mathcal{L}\left(\boldsymbol{\Theta}\right) = \sum\nolimits_{n=1}^{N} \left\|\mathbf{x}_n - \hat{\mathbf{x}}_n\right\|_2^2. \tag{8}$$

Because different AE models differ in their AE architectures and loss functions, we will discuss the specific architecture and loss functions for each reviewed DL model in ****Section 4.

Generative adversarial networks

GANs have been used for imputation, data generation and augmentation of the scRNA-seq analysis. Without loss of generality, the GAN, when applied to scRNA-seq, is designed to learn how to generate gene expression profiles from p_x, the distribution of $\mathbf{x}_n$. The vanilla GAN consists of two deep neural networks (DNNs) [48]. The first network is the generator$G_{\boldsymbol{\theta}}(\mathbf{z}_n, y_n)$ with parameter $\boldsymbol{\theta}$, a noise vector $\mathbf{z}_n$ from the distribution p_z and a class label

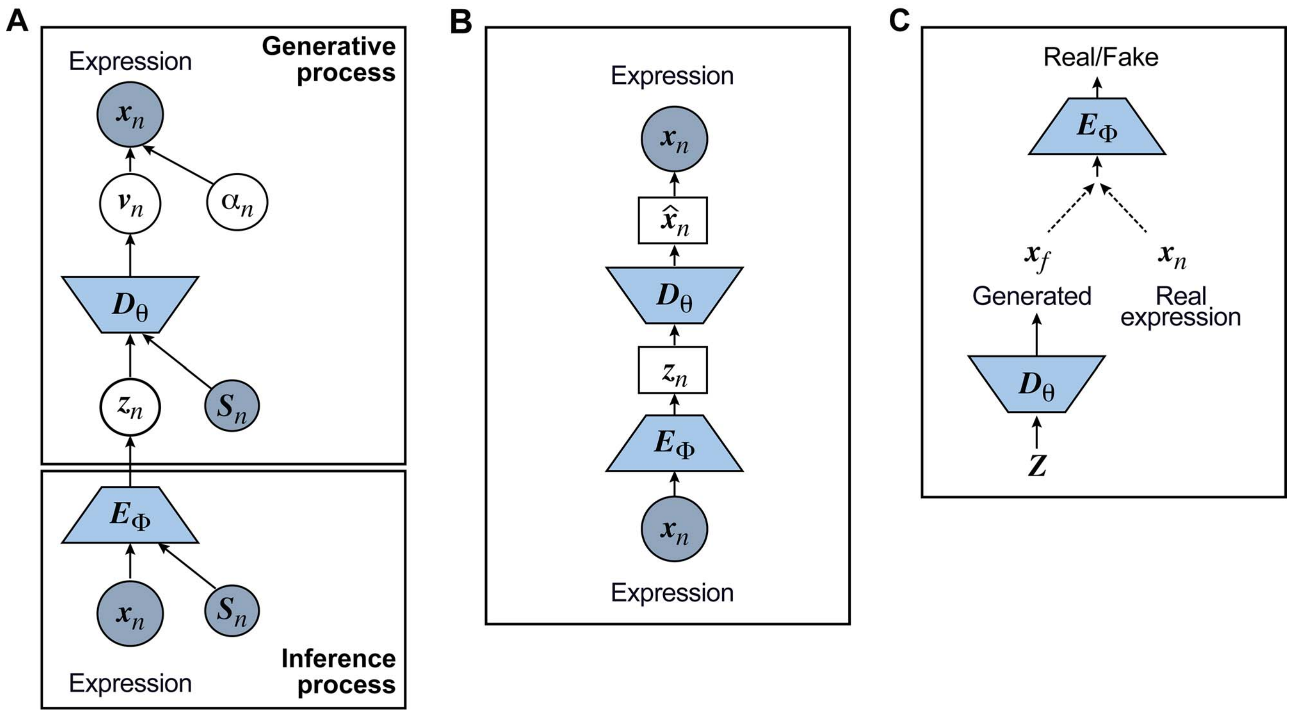

Figure 2. Graphical models of the major surveyed DL models including (**A**) VAE, (**B**) AE and (**C**) GAN.

y (e.g. cell type), and is trained to generate $\boldsymbol{x}_f$, a 'fake' gene expression (Figure 2C). The second network is the discriminator network $D_{\boldsymbol{\phi}_\mathrm{D}}$ with parameters $\boldsymbol{\phi}_\mathrm{D}$, trained to distinguish the 'real' $\boldsymbol{x}$ from fake $\boldsymbol{x}_f$ (Figure 2C). Both networks, $G_{\boldsymbol{\theta}}$ and $D_{\boldsymbol{\phi}_\mathrm{D}}$, are trained to outplay each other, resulting in a minimax game, in which $G_{\boldsymbol{\theta}}$ is forced by $D_{\boldsymbol{\phi}_\mathrm{D}}$ to produce better samples, which, when converge, can fool the discriminator $D_{\boldsymbol{\phi}_\mathrm{D}}$, thus becoming samples from p_x. The vanilla GAN suffers heavily from training instability and mode collapsing [49]. To that end, Wasserstein GAN (WGAN) [49] was developed with the WGAN loss [50]

$$L(\boldsymbol{\theta}) = \max_{\varnothing_\mathrm{D}} \sum_{n=1}^{N} D_{\varnothing_\mathrm{D}}(\mathbf{x}_n) - \sum_{n=1}^{N} D_{\varnothing_\mathrm{D}}(G_\theta(\mathbf{z}_n, y_n)). \quad (9)$$

Additional terms can also be added to Eq. (9) to constrain the functions of the generator. Training based on the WGAN loss in Eq. (9) amounts to a min-max optimization, which iterates between the discriminator and the generator, where each optimization is achieved by a stochastic gradient descent algorithm through backpropagation. The WGAN requires $D_{\boldsymbol{\phi}_\mathrm{D}}$ to be K-Lipschitz continuous [50], which can be satisfied by adding the gradient penalty to the WGAN loss [49]. Once the training is done, the generator $G_{\varnothing_G}$ can be used to generate gene expression profiles of new cells.

Supervised DL models

Supervised DL models, including DNNs, convolutional neural network (CNN) and capsule networks (CapsNet), have been used for cell-type identifications [51–53] and functional predictions [54]. The general supervised DL model F takes $\boldsymbol{x}_n$ as an input and outputs $p(y_n|\boldsymbol{x}_n)$, the probability of phenotype label y_n (e.g., a cell type) as

$$p(y_n|\boldsymbol{x}_n) = F(\boldsymbol{x}_n), \quad (10)$$

where F can be DNN, CNN or CapsNet. We omit the discussion of DNN and CNN as they are widely used in different applications and there are many excellent surveys on them [55]. We will focus our discussion on CasNet next.

A CasNet takes an expression $\boldsymbol{x}_n$ to first form a feature extraction network (consisting of L parallel single-layer neural networks) followed by a classification capsule network. Each of the L parallel feature extraction layers generates a primary capsule $\boldsymbol{u}_l \in \mathbb{R}^{dp}$ as

$$\boldsymbol{u}_l = \mathrm{ReLU}(\mathbf{W}_{P,l}\boldsymbol{x}_n)\ \forall l = 1, \ldots, L, \quad (11)$$

where $\mathbf{W}_{P,l} \in \mathbb{R}^{dp \times G}$ is the weight matrix. Then, the primary capsules are fed into the capsule network to compute K label capsules $\boldsymbol{v}_k \in \mathbb{R}^{d_t}$, one for each label, as

$$\boldsymbol{v}_k = squash\left(\sum_{l}^{L} c_{kl}\mathbf{W}_{kl}\boldsymbol{u}_l\right)\ \forall k = 1, \ldots, K, \quad (12)$$

where *squash* is the squashing function [56] to normalize the magnitude of its input vector to be less than one, $\mathbf{W}_{kl}$ is another trainable weight matrix and $c_{kl} \forall l = 1, \ldots, L$ are the coupling coefficients that represent the probability distribution of each primary capsule's impact on the predicted label k. Parameters c_{kl} are not trained but computed through the dynamic routing process proposed

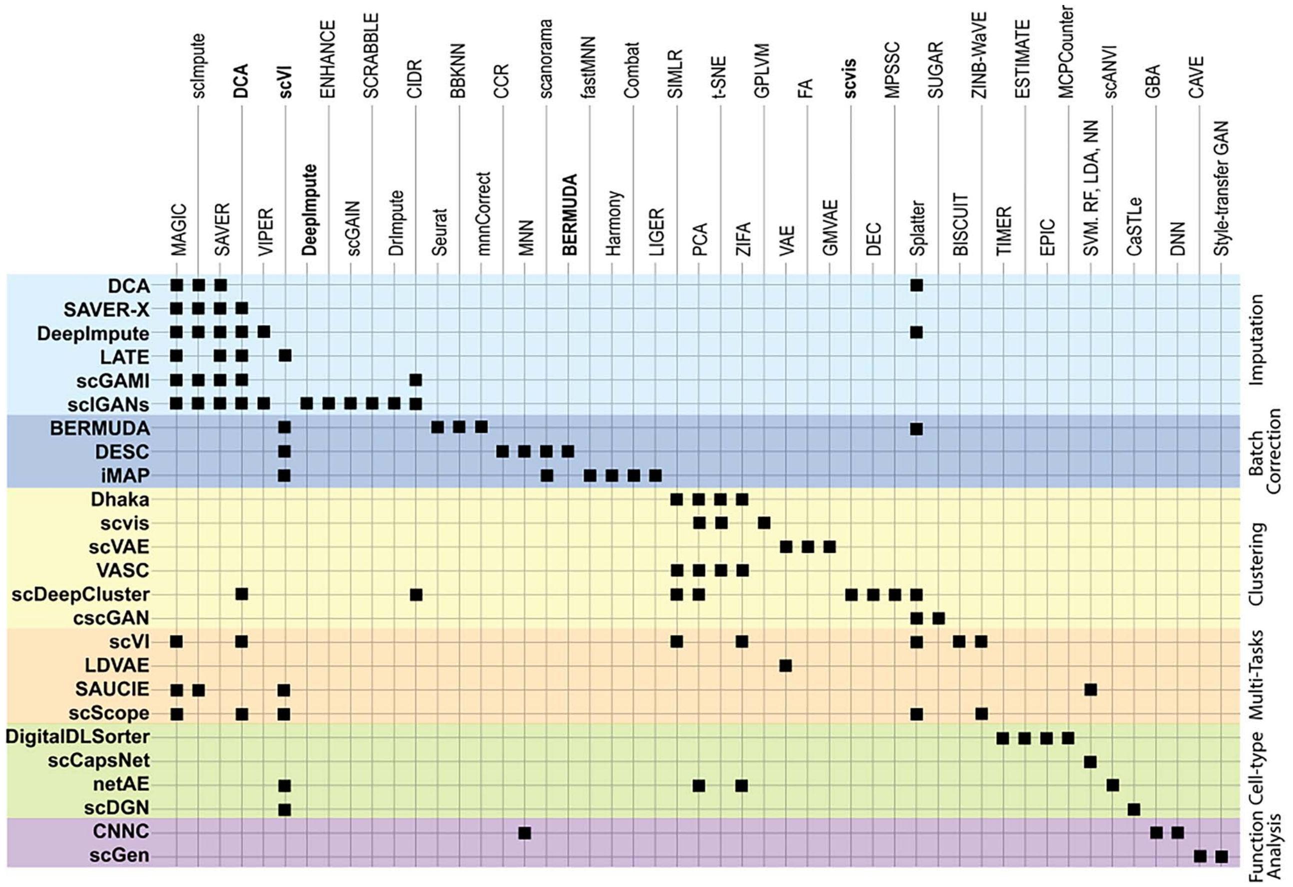

		MAGIC	scImpute	SAVER	DCA	VIPER	scVI	DeepImpute	ENHANCE	scGAIN	SCRABBLE	DrImpute	CIDR	Seurat	BBKNN	mnnCorrect	CCR	MNN	scanorama	BERMUDA	fastMNN	Harmony	Combat	LIGER	SIMLR	PCA	t-SNE	ZIFA	GPLVM	VAE	FA	GMVAE	scvis	DEC	MPSSC	Splatter	SUGAR	BISCUIT	ZINB-WaVE	TIMER	ESTIMATE	EPIC	MCPCounter	SVM. RF, LDA, NN	scANVI	CaSTLe	GBA	DNN	CAVE	Style-transfer GAN
Imputation	DCA	■	■	■																																■														
Imputation	SAVER-X	■	■	■	■																																													
Imputation	DeepImpute	■	■	■	■	■																														■														
Imputation	LATE	■		■	■		■																																											
Imputation	scGAMI	■	■	■	■								■																																					
Imputation	scIGANs	■	■	■	■	■		■	■	■	■	■	■																																					
Batch Correction	BERMUDA						■							■	■	■																				■														
Batch Correction	DESC						■										■	■	■	■																														
Batch Correction	iMAP						■												■		■	■	■	■																										
Clustering	Dhaka																								■	■	■	■																						
Clustering	scvis																									■	■		■																					
Clustering	scVAE																													■	■	■																		
Clustering	VASC																								■	■	■	■																						
Clustering	scDeepCluster				■								■												■	■							■	■	■	■														
Clustering	cscGAN																																			■	■													
Multi-Tasks	scVI	■			■																				■			■								■		■	■											
Multi-Tasks	LDVAE																													■																				
Multi-Tasks	SAUCIE	■	■				■																																					■						
Multi-Tasks	scScope	■			■		■																													■			■											
Cell-type	DigitalDLSorter																																							■	■	■	■							
Cell-type	scCapsNet																																											■						
Cell-type	netAE						■																			■		■																	■					
Cell-type	scDGN						■																																							■				
Function Analysis	CNNC																	■																													■	■		
Function Analysis	scGen																																																■	■

Figure 3. Algorithm comparison grid. DL methods surveyed in the paper are listed on the left-hand side, and some in the column. Algorithms selected to compare in each DL method are marked by '■' at each cross-point.

in the original capsule networks [52]. The magnitude of each capsule $\boldsymbol{v}_k$ represents the probability of predicting label k for input $\boldsymbol{x}_n$. Once trained, the important primary capsules for each label and then the most significant genes for each important primary capsule can be used to interpret biological functions associated with the prediction.

The training of the supervised models for classification overwhelmingly minimizes the cross-entropy loss by stochastic gradient descent computed by a back-propagation algorithm.

Survey of DL models for scRNA-seq analysis

In this section, we survey applications of DL models for scRNA-seq analysis. To better understand the relationship between the problems that each surveyed work addresses and the key challenges in the general scRNA-seq processing pipeline, we divide the survey into sections according to steps in the scRNA-seq processing pipeline illustrated in Figure 1. For each DL model, we present the model details under the general model framework introduced in Section 3 and discuss the specific loss functions. We also survey the evaluation metrics and summarize the evaluation results. To facilitate cross-references of the information, we summarized all algorithms reviewed in this section in **Table 1** and tabulated the datasets and evaluation metrics used in each paper in Tables 3 and 8**.** We also listed in Figure 3 all other algorithms against which each surveyed method evaluated, highlighting the extensiveness that these algorithms were assessed for their performance.

Imputation

DCA: Deep count AE

DCA [18] is an AE for imputation (Figures 2B and 4B) and has been integrated into the Scanpy framework.

Model

DCA models UMI counts with missing values using the ZINB distribution

$$p\left(x_{gn}|\boldsymbol{\Theta}\right) = \pi_{gn}\delta(0) + \left(1-\pi_{gn}\right) NB\left(\nu_{gn}, \alpha_{gn}\right),$$
$$\text{for } g = 1, \dots G; n = 1, \dots N, \tag{13}$$

where $\delta(\cdot)$ is a Dirac delta function, $NB(\cdot,\cdot)$ denotes the negative binomial distribution and $\pi_{gn}, \nu_{gn}, \alpha_{gn}$, representing dropout rate, mean and dispersion, respectively, are functions of the output ($\hat{\mathbf{x}}_n$) of the decoder in the DCA as follows:

$$\boldsymbol{\pi}_n = sigmoid\left(\mathbf{W}_\pi \hat{\mathbf{x}}_n\right); \boldsymbol{\nu}_n = \exp\left(\mathbf{W}_{\boldsymbol{\nu}} \hat{\mathbf{x}}_n\right); \boldsymbol{\alpha}_n = \exp\left(\mathbf{W}_{\boldsymbol{\alpha}} \hat{\mathbf{x}}_n\right), \tag{14}$$

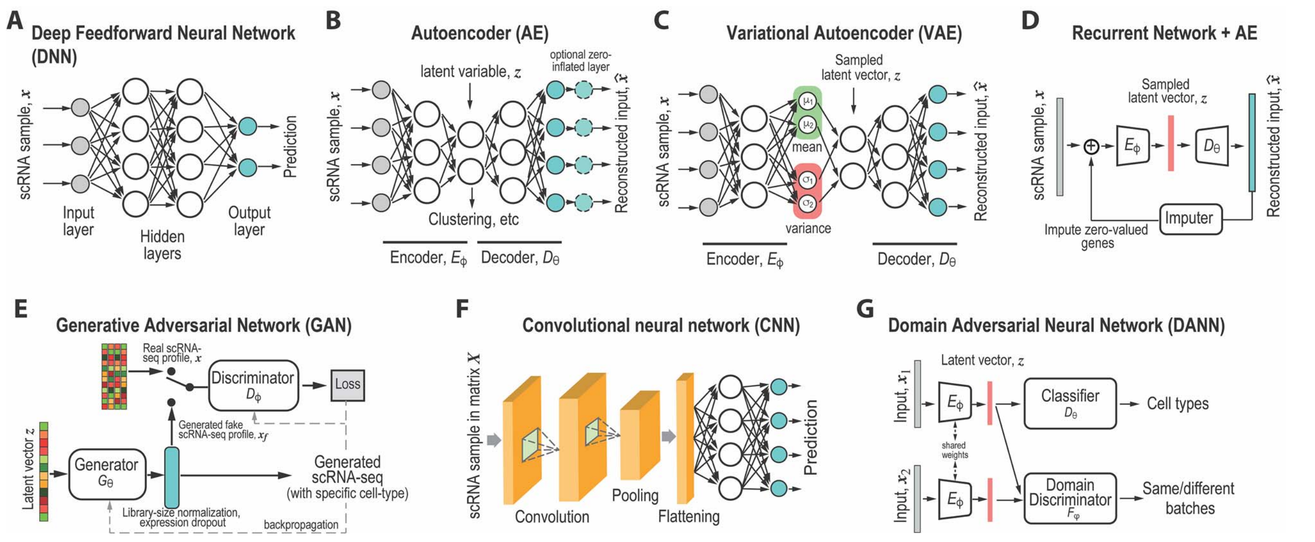

Figure 4. DL model network illustration. (**A**) DNN, (**B**) AE, (**C**) VAE, (**D**) AE with recursive imputer, (**E**) GAN, (**F**) CNN and (**G**) domain adversarial neural network.

where $\mathbf{W}_\pi$, $\mathbf{W}_\upsilon$ and $\mathbf{W}_\alpha$ are additional weights to be estimated. The DCA encoder and decoder follow the general AE formulation as in Eq. (7) but the encoder takes the normalized, log-transformed expression as input. To train the model, DCA uses a constrained log-likelihood as the loss function

$$L(\boldsymbol{\Theta}) = \sum_{n=1}^{N}\sum_{g=1}^{G}\left(-logp\left(x_{gn}|\boldsymbol{\Theta}\right) + \lambda\pi_{gn}^2\right), \qquad (15)$$

with $\boldsymbol{\Theta} = \{\boldsymbol{\theta}, \boldsymbol{\phi}, \mathbf{W}_\pi, \mathbf{W}_\upsilon, \mathbf{W}_\alpha\}$. Once the DCA is trained, the mean counts $\boldsymbol{\upsilon}_n$ are used as the denoised and imputed counts for cell n.

Results

For evaluation, DCA was compared with other methods using simulated data (using Splatter R package), and real bulk transcriptomics data from a developmental *Caenorhabditis elegans* time-course experiment were used with added simulating single-cell specific noise. Gene expression was measured from 206 developmentally synchronized young adults over a 12-h period (*C. elegans*). Single-cell specific noise was added *in silico* by genewise subtracting values drawn from the exponential distribution such that 80% of values were zeros. The paper analyzed the Bulk contains less noise than single-cell transcriptomics data and can thus aid in evaluating single-cell denoising methods by providing a good ground truth model. The authors also did a comparison of other methods including SAVER [36], scImpute [37] and MAGIC [57]. DCA denoising recovered original time-course gene expression pattern while removing single-cell specific noise. Overall, DCA demonstrated the strongest recovery of the top 500 genes most strongly associated with development in the original data without noise; DCA was shown to outperform other existing methods in capturing cell population structure in real data using PBMC, CITE-seq, runtime scales linearly with the number of cells.

SAVER-X: *Single-cell analysis via expression recovery harnessing external data*

SAVER-X [58] is an AE model (Figures 2B and 4B) developed to denoise and impute scRNA-seq data with transfer learning from other data resources.

Model

SAVER-X decomposes the variation in the observed counts $\boldsymbol{x}_n$ with missing values into three components: (i) predictable structured component representing the shared variation across genes, (ii) unpredictable cell-level biological variation and gene-specific dispersions and (iii) technical noise. Specifically, x_{gn} is modeled as a Poisson–Gamma hierarchical model

$$\begin{aligned} p\left(x_{gn}|\boldsymbol{\Theta}\right) &= \text{Poisson}\left(l_n x'_{gn}\right), p\left(x'_{gn}|\nu_{gn}, \alpha_g\right) \\ &= \text{Gamma}\left(\nu_{gn}, \alpha_g \nu_{gn}^2\right), \end{aligned} \qquad (16)$$

where l_n is the sequencing depth of cell n, ν_{gn} is the mean and α_g is the dispersion. This Poisson–Gamma mixture is an equivalent expression to the NB distribution, and thus, the ZINB distribution as Eq. (13) is adopted to model missing values.

The loss is similar to Eq. (15). However, ν_{gn} is initially learned by an AE pre-trained using external datasets from an identical or similar tissue and then transferred to $\boldsymbol{x}_n$ to be denoised. Such transfer learning can be applied to data between species (e.g. human and mouse in the study), cell types, batches and single-cell profiling technologies. After ν_{gn} is inferred, SAVER-X generates the final denoised data $\hat{x}_{gn}$ by an empirical Bayesian shrinkage.

Results

SAVER-X was applied to multiple human single-cell datasets of different scenarios: (i) T-cell subtypes, (ii) a cell type (CD4+ regulatory T cells) that was absent from the pretraining dataset, (iii) gene-protein correlations of CITE-seq data and (iv) immune cells of primary breast cancer samples with a pretraining on normal immune cells. SAVER-X with pretraining on HCA and/or PBMCs outperformed the same model without pretraining and other denoising methods, including DCA [28], scVI [17], scImpute [37] and MAGIC [57]. The model achieved promising results even for genes with very low UMI counts. SAVER-X was also applied for a cross-species study in which the model was pre-trained on a human or mouse dataset and transferred to denoise another. The results demonstrated the merit of transferring public data resources to denoise in-house scRNA-seq data even when the study species, cell types or single-cell profiling technologies are different.

DeepImpute: DNN imputation

DeepImpute [20] imputes genes in a divide-and-conquer approach, using a bank of DNN models (Figure 4A) with 512 output, each to predict gene expression levels of a cell.

Model

For each dataset, DeepImpute selects to impute a list of genes or highly variable genes (variance over mean ratio, default = 0.5). Each sub-neural network aims to understand the relationship between the input genes and a subset of target genes. Genes are first divided into N random subsets of 512 target genes. For each subset, a two-layer DNN is trained where the input includes genes that are among the top 5 best-correlated genes to target genes but not part of the target genes in the subset. The loss is defined as the weighted MSE

$$\mathcal{L}(\boldsymbol{\Theta}) = \sum \mathbf{x}_n \left(\mathbf{x}_n - \hat{\mathbf{x}}_n\right)^2, \tag{17}$$

which gives higher weights to genes with higher expression values.

Result

DeepImpute had the highest overall accuracy and offered shorter computation time with less demand on computer memory than other methods such as MAGIC, DrImpute, ScImpute, SAVER, VIPER and DCA. Using simulated and experimental datasets (Table 3), DeepImpute showed benefits in improving clustering results and identifying significantly differentially expressed genes. DeepImpute and DCA show overall advantages over other methods and between which DeepImpute performs even better. The properties of DeepImpute contribute to its superior performance include (i) a divide-and-conquer approach which contrary to an AE as implemented in DCA, resulting in a lower complexity in each sub-model and stabilizing neural networks and (ii) the subnetworks are trained without using the target genes as the input which reduces overfitting while enforcing the network to understand true relationships between genes.

LATE: Learning with AE

LATE [59] is an AE (Figures 2B and 4B) whose encoder takes the log-transformed expression as input.

Model

LATE sets zeros for all missing values and generates the imputed expressions. LATE minimizes the MSE loss as Eq. (8). One issue is that some zeros could be real and reflect the actual lack of expressions.

Result

Using synthetic data generated from pre-imputed data followed by random dropout selection at different degrees, LATE outperforms other existing methods such as MAGIC, SAVER, DCA and scVI, particularly when the ground truth contains only a few or no zeros. However, when the data contain many zero expression values, DCA achieved a lower MSE than LATE, although LATE still has a smaller MSE than scVI. This result suggests that DCA likely does a better job identifying true zero expressions, partly because LATE does not make assumptions on the statistical distributions of the single-cell data that potentially have inflated zero counts.

scGMAI

Technically, scGMAI [60] is a model for clustering but it includes an AE (Figures 2B and 4B) in the first step to combat dropout.

Model

To impute the missing values, scGMAI applies an AE like LATE to reconstruct log-transformed expressions with dropout but chooses a smoother Softplus activation function instead. The MSE loss as in Eq. (8) is adopted.

After imputation, scGMAI uses fast independent component analysis (ICA) on the AE reconstructed expressions to reduce the dimension and then applies a Gaussian mixture model on the ICA reduced data to perform the clustering.

Results

To assess the performance, the AE in scGMAI was replaced by five other imputation methods including SAVER [36], MAGIC [57], DCA [28], scImpute [37] and CIDR [61]. A scGMAI implementation without AE was also compared. Seventeen scRNA-seq data (part of them are listed in Tables 4 and 5 as marked) were used to evaluate cell clustering performances. The results indicated that the AEs significantly improved the clustering performance in 8 of 17 scRNA-seq datasets.

scIGANs

Imputation approaches based on information from cells with similar expressions suffer from oversmoothing,

Table 2. Comparison of DL algorithms reviewed in the paper

App	Algorithm	Feature	Application notes
Imputation			
	DCA	• Strongest recovery of the top 500 genes • Choices of noise models, including NB and ZINB • Outperform other existing methods in capturing cell population structure	• AE integrated into the Scanpy framework • High scalability of AE, up to millions of cells • This method was compared to SAVER, scImpute and MAGIC
	SAVER-X	• Pretraining from existing data sets (transfer learning) • Decomposes the variation into three components	• SAVER-X pretraining on PBMCs outperformed other denoising methods, including DCA, scVI, scImpute and MAGIC • SAVER-X was also applied for cross-species analysis
	DeepImpute	• Divide-and-conquer approach, using a bank of DNN models • Reduced complexity by learning smaller sub-network • Minimized overfitting by removing target genes from input	• DeepImpute had the highest overall accuracy and offered shorter computation time than other methods such as MAGIC, DrImpute, ScImpute, SAVER, VIPER and DCA • DeepImpute showed benefits in improving clustering results and identifying significantly differentially expressed genes • Scalable and faster training time
	LATE	• Takes the log-transformed expression as input • No explicit distribution assumption on input data	• LATE outperforms other existing methods like MAGIC, SAVER, DCA, scVI, particularly when the ground truth contains only a few or no zeros • Better scalability than DCA and scVI up to 1.3 million cells with 10 K genes
	scGAMI	• A model designed for clustering but it includes an AE • Uses fast ICA algorithm: FastICA	• Significantly improved the clustering performance in eight of seventeen selected scRNA-seq datasets • scGMI's scalability needs to be improved
	scIGANs	• Trains a GAN model to generate samples with imputed expressions	• This framework forces the model to reconstruct the real samples and discriminate between real and generated samples. • Best reported performance in clustering compared to DCA, DeepImpute, SAVER, scImpute, MAGIC • Scalable over 100 K cells, also robust to small datasets
Batch correction			
	BERMUDA	• Preserves batch-specific biological signals through transfer-learning Preserves batch-specific cell populations	• Outperform other methods like mnnCorrect, BBKNN, Seurat and scVI • Removes batch effects even when the cell population compositions across different batches are vastly different • Scalable by using mini-batch gradient descent algorithm during training
	DESC	• Removes batch effect through clustering with the hypothesis that batch differences in expressions are smaller than true biological variations • Does not require explicit batch information for batch removal	• DESC is effective in removing the batch effect, whereas CCA, MNN, Seurat 3.0, scVI, BERMUDA and scanorama were sensitive to batch definitions • DESC is biologically interpretable and can reveal both discrete and pseudo-temporal structures of cells • Small memory footprint and GPU enabled

(*Continued*)

Table 2. Continued

App	Algorithm	Feature	Application notes
	iMAP	• iMAP combines AE and GAN for batch effect removal • It consists of two processing stages, each including a separate DL model	• iMAP was shown to separate the batch-specific cell types but mix batch shared cell types and outperformed other existing batch correction methods including Harmony, scVI, fastMNN, Seurat • Capable handling datasets from Smart-seq2 and 10X Genomics platforms • Demonstrated the stability over hyperparameters, and scalability for thousands of cells.
Clustering, latent representation, dimension reduction and data augmentation			
	Dhaka	• It was proposed to reduce the dimension of scRNA-seq data for efficient stratification of tumor subpopulations	• Dhaka was shown to have an ARI higher than most other comparing methods including t-SNE, PCA, SIMLR, NMF, an AE, MAGIC and scVI • Dhaka can represent an evolutionary trajectory
	scvis	• VAE network that learns low-dimensional representations • Capture both local and global neighboring structures	• scvis was tested on the simulated data and outperformed *t*-SNE • scvis is much more scalable than BH *t*-SNE (*t*-SNE takes O(M log(M)) time and O(M log(M)) space) for very large dataset (>1 million cells)
	scVAE	• scVAE includes multiple VAE models for denoising gene expression levels and learning the low-dimensional latent representation • Gaussian Mixture VAE (GMVAE) with negative binomial distribution achieved the highest lower bound and ARI	• GMVAE was also compared with Seurat and shown to perform better, however, scVAE performed no better than scVI or scvis • Algorithm applicable to large datasets with million cells
	VASC	• Another VAE for dimension reduction and latent representation • Explicitly model dropout with a Zero-inflated layer	• VASC was compared with PCA, *t*-SNE, ZIFA and SIMLR on 20 datasets • In the study of embryonic development from zygote to blast cells, VASC shthe owed better performance to model embryo developmental progression • VASC is reported to handle a large number of cells or cell types • Demonstrated model stability
	scDeepClus-ter	• AE network that simultaneously learns feature representation and performs clustering via explicit modeling of cell clusters	• It was tested on the simulation data with different dropout rates and compared with DCA, MPSSC and SIMLR CIDR, PCA + k-mean, scvis and DEC significantly outperforming them • Running time of scDeepCluster scales linearly with the number of cells, suitable for large scRNA-seq datasets

(Continued)

Table 2. Continued

App	Algorithm	Feature	Application notes
	cscGAN	• It was designed to augment the existing scRNA-seq samples by generating expression profiles of specific cell types or subpopulations • The cscGAN learns the expression patterns of a specific subpopulation (few cells) and simultaneously learns the cells from all populations (a large number of cells).	• cscGAN was shown to generate high-quality scRAN-seq data for specific cell types. • The augmentation in this method improved the identification of rare cell types and the ability to capture transitional cell states from trajectory analysis • Better scalability than SUGAR (Synthesis Using Geometrically Aligned Random-walks) • Capable re-establish developmental trajectories through pseudo-time analysis via cscGAN data augmentation
Multi-functional models			
	scVI	• Designed to address a range of fundamental analysis tasks, including batch correction, visualization, clustering and differential expression • Integrated a normalization procedure and batch correction	• ScVI was shown to be faster than most non-DL algorithms and scalable to handle twice as many cells as non-DL algorithms with a fixed memory • For imputation, ScVI, together with other ZINB-based models, performed better than methods using alternative distributions • Similar scalability as DCA
	LDVAE	• Adaption of scVI to improve the model interpretability	• For LDVAE the variations along the different axes of the latent variable establish direct linear relationships with input genes.
	SAUCIE	• It is applied to the normalized data instead of count data	• Results showed that SAUCIE had a better or comparable performance with other approaches • SAUCIE has better scalability and faster runtimes than any of the other models • Applications with single-cell CyTOF datasets
	scScope	• AE with recurrent steps designed for imputation and batch correction	• It was compared with PCA, MAGIC, ZINB-WaVE, SIMLR, AE, scVI and DCA • Efficiently identify cell subpopulations from complex datasets with high dropout rates, large numbers of subpopulations and rare cell types • For scalability and training speed, scScope was shown to offer scalability (for >100 K cells) with high efficiency (faster than most of the approaches)
Cell type Identification			
	DigitalDL-Sorter	• A deconvolution model with 4-layer DNN • Designed to identify and quantify the immune cells infiltrated in tumors captured in bulk RNA-seq, utilizing single-cell RNA-seq data	• DigitalDLSorter achieved excellent agreement (linear correlation of 0.99 for colorectal cancer, and good agreement in quadratic relationship for breast cancer) at predicting cell type proportion.
	scCapsNet	• It takes log-transformed, normalized expressions as input and follows the general CapsNet model	• Interpretable capsule network designed for cell-type prediction • scCapsNet makes the deep-learning black box transparent through the direct interpretation of internal parameters

(Continued)

Table 2. Continued

App	Algorithm	Feature	Application notes
	netAE	• VAE-based semi-supervised cell-type prediction model • Aiming at learning a low dimensional space from which the original space can be accurately reconstructed	• Deals with scenarios of having a small number of labeled cells. • netAE outperformed most of the baseline methods including scVI, ZIFA, PCA and AE as well as a semi-supervised method scANVI
	scDGN	• scDGN takes the log-transformed, normalized expression as the input • Supervised domain adversarial network	• scDGN was tested for classifying cell types and aligning batches • scDGN outperformed many DL and traditional ML methods in classification accuracy, including DNN, CaSTLe, MNN, scVI and Seurat
Function analysis			
	CNNC	• CNNC takes expression levels of two genes from many cells and transforms them into a 32 × 32 image-like NEPDF • Inferring causal interactions between genes from scRNA-seq	• CNNC outperforms prior methods for inferring TF–gene and PPIs, causality inference and functional assignments • Was shown to have more than 20% higher AUPRC than other methods and reported almost no false-negative for the top 5% predictions
	scGen	• ScGen follows the general VAE for scRNA-seq data but uses the 'latent space arithmetics' to learn perturbations' response • Designed to learn cell response to certain perturbation (drug treatment, gene knockout, etc.)	• Compared with other methods including CVAE, style transfer GAN, linear approaches based on VA and PCA + VA, scGen predicted full distribution of ISG15 gene (strongest regulated gene by IFN-b) response to IFN- b • scGen can be used to translate the effect of a stimulation trained in study A to how stimulated cells would look in study B, given a control sample set

Abbreviation: NB: negative binomial distribution.

especially for rare cell types. scIGANs [19] is a GAN-based imputation algorithm (Figures 2C and 4E), which overcomes this problem by training a GAN model to generate samples with imputed expressions.

Model

scIGAN takes the image-like reshaped gene expression data $\boldsymbol{x}_n$ as input. The model follows a BEGAN [62] framework, which replaces the GAN discriminator D with a function $R_{\o_R}$ to compute the reconstruction MSE. Then, the Wasserstein distance loss between the reconstruction errors between the real and generated samples is computed

$$L(\boldsymbol{\theta}, \boldsymbol{\Phi}) = \max_{\o_R} \sum_{n=1}^{N} R_{\o_R}(\boldsymbol{x}_n) - \sum_{n=1}^{N} R_{\o_R}\left(G_\theta\left(E_{\boldsymbol{\Phi}}(\boldsymbol{x}_n), y\right)\right). \tag{18}$$

This framework forces the model to meet two computing objectives, i.e. reconstructing the real samples and discriminating between real and generated samples. Proportional Control Theory was applied to balance these two goals during the training [62].

After training, the decoder G_θ is used to generate new samples of a specific cell type. Then, the k-nearest neighbors (KNNs) approach is applied to the real and generated samples to impute the real samples' missing expressions.

Results

scIGANs were first tested on simulated samples with different dropout rates. Performance of rescuing the correct clusters was compared with 11 existing imputation approaches including DCA, DeepImpute, SAVER, scImpute, MAGIC, etc. scIGANs reported the best performance for all metrics. scIGAN was next evaluated for its ability to correctly cluster cell types on the Human brain scRNA-seq data, which showed superior performance than existing methods again. scIGANs were then evaluated for identifying cell-cycle states using scRNA-seq datasets from mouse embryonic stem cells. The results showed that scIGANs outperformed competing existing approaches for recovering subcellular states of cell cycle dynamics. scIGANs were further shown to improve the identification of differentially expressed genes and enhance the inference of cellular trajectory using time-course scRNA-seq data from the differentiation from H1

Table 3. Simulated single-cell data/algorithms

Title	Algorithm	# Cells	Simulation methods	Reference
Splatter	DCA, DeepImpute, PERMUDA, scDeepCluster, scVI, scScope, solo	∼2000	Splatter/R	[84]
CIDR	sclGAN	50	CIDR simulation	[61]
NB + dropout	Dhaka	500	Hierarchical model of NB/Gamma + random dropout	
Bulk RNA-seq	SAUCIE	1076	1076 CCLE bulk RNAseq + dropout conditional on the expression level	
SIMLR	scScope	1 million	SIMLR, high-dimensional data generated from latent vector	[44]
SUGAR	cscGAN	3000	Generating high dimensional data that follows a low dimensional manifold	[85]

Table 4. Human single-cell data sources used by different DL algorithms

Title	Algorithm	Cell origin	# Cells	Data sources	Reference
68 k PBMCs	DCA SAVER-X LATE, scVAE, scDeepCluster, scCapsNet, scDGN	Blood	68 579	10× Single Cell Gene Expression Datasets	
Human pluripotent	DCA	hESCs	1876	GSE102176	[128]
CITE-seq	SAVER-X	Cord blood mononuclear cells	8005	GSE100866	[129]
Midbrain and Dopaminergic Neuron Development	SAVER-X	Brain/ embryo ventral midbrain cells	1977	GSE76381	[130]
HCA	SAVER-X	Immune cell, Human Cell Atlas	500 000	HCA data portal	
Breast tumor	SAVER-X	Immune cell in tumor micro-environment	45 000	GSE114725	[131]
293 T cells	DeepImpute, iMAP	Embryonic kidney	13 480	10X Single Cell Gene Expression Datasets	
Jurkat	DeepImpute, iMAP	Blood/ lymphocyte	3200	10X Single Cell Gene Expression Datasets	
ESC, Time-course	scGAN	ESC	350 758	GSE75748	[132]
Baron-Hum-1	scGMAI, VASC	Pancreatic islets	1937	GSM2230757	[133]
Baron-Hum-2	scGMAI, VASC	Pancreatic islets	1724	GSM2230758	[133]
Camp	scGMAI, VASC	Liver cells	303	GSE96981	[134]
CEL-seq2	PERMUDA, DESC	Pancreas/Islets of Langerhans		GSE85241	[135]
Darmanis	scGMAI, sclGAN, VASC	Brain/cortex	466	GSE67835	[136]
Tirosh-brain	Dhaka, scvis	Oligodendroglioma	>4800	GSE70630	[137]
Patel	Dhaka	Primary glioblastoma cells	875	GSE57872	[138]
Li	scGMAI, VASC	Blood	561	GSE146974	[67]
Tirosh-skin	scvis	melanoma	4645	GSE72056	[73]
xenograft 3, and 4	Dhaka	Breast tumor	∼250	EGAS00001002170	[74]
Petropoulos	VASC/netAE	Human embryos	1529	E-MTAB-3929	
Pollen	scGMAI, VASC		348	SRP041736	[139]
Xin	scGMAI, VASC	Pancreatic cells (α-, β-, δ-)	1600	GSE81608	[140]
Yan	scGMAI, VASC	embryonic stem cells	124	GSE36552	[141]
PBMC3k	VASC, scVI	Blood	2700	SRP073767	[99]
CyTOF, Dengue	SAUCIE	Dengue infection	11 M, ∼42 antibodies	Cytobank, 82 023	[15]
CyTOF, ccRCC	SAUCIE	Immunue profile of 73 ccRCC patients	3.5 M, ∼40 antibodies	Cytobank: 875	[142]
CyTOF, breast	SAUCIE	3 patients		Flow Repository: FR-FCM-ZYJP	[131]
Chung, BC	DigitalDLSorter	Breast tumor	515	GSE75688	[93]
Li, CRC	DigitalDLSorter	Colorectal cancer	2591	GSE81861	[94]
Pancreatic datasets	scDGN	Pancreas	14 693	SeuratData	
Kang, PBMC	scGen	PBMC stimulated by INF-β	∼15 000	GSE96583	[115]

Table 5. Mouse single-cell data sources used by different DL algorithms

Title	Algorithm	Cell origin	# Cells	Data Sources	Reference
Brain cells from E18 mice	DCA, SAUCIE	Brain Cortex	1 306 127	10×: Single Cell Gene Expression Datasets	
Midbrain and Dopaminergic Neuron Development	SAVER-X	Ventral Midbrain	1907	GSE76381	[130]
Mouse cell atlas	SAVER-X		405 796	GSE108097	[143]
neuron9k	DeepImpute	Cortex	9128	10×: Single Cell Gene Expression Datasets	
Mouse Visual Cortex	DeepImpute	Brain cortex	114 601	GSE102827	[144]
murine epidermis	DeepImpute	Epidermis	1422	GSE67602	[145]
myeloid progenitors	LATE DESC, SAUCIE	Bone marrow	2730	GSE72857	[146]
Cell-cycle	scIGAN	mESC	288	E-MTAB-2805	[147]
A single-cell survey		Intestine	7721	GSE92332	[119]
Tabula Muris	iMAP	Mouse cells	>100 K		
Baron-Mou-1	VASC	Pancreas	822	GSM2230761	[133]
Biase	scGMAI, VASC	Embryos/SMARTer	56	GSE57249	[148]
Biase	scGMAI, VASC	Embryos/Fluidigm	90	GSE59892	[148]
Deng	scGMAI, VASC	Liver	317	GSE45719	[149]
Klein	VASC scDeepCluster scIGAN	Stem Cells	2717	GSE65525	[150]
Goolam	VASC	Mouse Embryo	124	E-METAB-3321	[151]
Kolodziejczyk	VASC	mESC	704	E-MTAB-2600	[152]
Usoskin	VASC	Lumbar	864	GSE59739	[153]
Zeisel	VASC, scVI, SAUCIE, netAE	Cortex, hippocampus	3005	GSE60361	[154]
Bladder cells	scDeepCluster	Bladder	12 884	GSE129845	[155]
HEMATO	scVI	Blood cell	>10 000	GSE89754	[156]
retinal bipolar cells	scVI, scCapsNet SAUCIE	retinal	~25 000	GSE81905	[100]
Embryo at 9 time points	LDAVE	embryos from E6.5 to E8.5	116 312	GSE87038	[157]
Embryo at 9 time points	LDAVE	embryos from E9.5 to E13.5	~2 millions	GSE119945	[158]
CyTOF,	SAUCIE	Mouse thymus	200 K, ~38 antibodies	Cytobank: 52942	[159]
Nestorowa	netAE	hematopoietic stem and progenitor cells	1920	GSE81682	[160]
small intestinal epithelium	scGen	Infected with Salmonella and worm *H. polygyrus*	1957	GSE92332	[119]

ESC to definitive endoderm cells (DECs). Finally, scIGAN was also shown to scale to scRNA-seq methods and data sizes.

Batch effect correction

BERMUDA: Batch Effect ReMoval Using Deep AEs

BERMUDA [63] deploys a transfer-learning method (Figures 2B and 4B) to remove the batch effect. It performs correction to the shared cell clusters among batches and therefore preserves batch-specific cell populations.

Model

BERMUDA is an AE that takes normalized, log-transformed expression as input. Its consists of two parts as

$$L(\mathbf{\Theta}) = \mathcal{L}(\mathbf{\Theta}) + \lambda L_{\mathrm{MMD}}(\mathbf{\Theta}), \qquad (19)$$

where $\mathcal{L}(\mathbf{\Theta})$ is the MSE loss and L_{MMD} is the maximum mean discrepancy (MMD) [64] loss that measures the differences in distributions between pairs of similar cell clusters shared among batches as

$$L_{\mathrm{MMD}}(\mathbf{\Theta}) = \sum\nolimits_{i_a,i_b,j_a,j_b} M_{i_a,j_a,i_b,j_b} \mathrm{MMD}\left(\mathbf{z}_{i_a,j_a}, \mathbf{z}_{i_b,j_b}\right), \qquad (20)$$

where $\mathbf{z}_{i,j}$ is the latent variable of $\mathbf{x}_{i,j}$, the input expression of a cell from cluster j of batch i, M_{i_a,j_a,i_b,j_b} is 1 if cluster i_a of batch j_a and cluster i_b of batch j_b are determined to be similar by MetaNeighbor [65] and 0, otherwise. The **MMD** equals zero when the underlying distributions of the observed samples are the same.

Results

BERMUDA was shown to outperform other methods such as MNNCorrect [32], BBKNN [66], Seurat [10] and scVI [17] in removing batch effects on simulated and human pancreas data while preserving batch-specific biological signals. BERMUDA provides several improvements compared with existing methods: (i) capable of removing

Table 6. Single-cell data derived from other species

Title	Algorithm	Species	Tissue	# Cells	SRA/GEO	Reference
Worm neuron cells [a]	scDeepCluster	*C. elegans*	Neuron	4186	GSE98561	[161]
Cross species, stimulation with LPS and dsRNA	scGen	Mouse, rat, rabbit and pig	bone marrow-derived phagocyte	5000–10 000 /species	13 accessions in ArrayExpress	[120]

[a]Processed data are available at https://github.com/ttgump/scDeepCluster/tree/master/scRNA-seq%20data

batch effects even when the cell population compositions across different batches are vastly different and (ii) preserving batch-specific biological signals through transfer-learning which enables discovering new information that might be hard to extract by analyzing each batch individually.

DESC: Batch correction based on clustering

DESC [67] is an AE model (Figures 2B and 4B) that removes batch effect through clustering with the hypothesis that batch differences in expressions are smaller than true biological variations between cell types, and, therefore, properly performing clustering on cells across multiple batches can remove batch effects without the need to define batches explicitly.

Model

DESC has a conventional AE architecture. Its encoder takes normalized, log-transformed expression and uses decoder output, $\hat{\mathbf{x}}_n$ as the reconstructed gene expression, which is equivalent to a Gaussian data distribution with $\hat{\mathbf{x}}_n$ being the mean. The loss function is similar to Eq. (19) and except that the second loss L_c is the clustering loss that regularizes the learned feature representations to form clusters as in the deep embedded clustering [68]. The model is first trained to minimize $\mathcal{L}(\boldsymbol{\Theta})$ only to obtain the initial weights before minimizing the combined loss. After the training, each cell is assigned with a cluster ID.

Results

DESC was applied to the macaque retina dataset, which includes animal level, region level and sample-level batch effects. The results showed that DESC is effective in removing the batch effect, whereas CCA [33], MNN [32], Seurat 3.0 [10], scVI [17], BERMUDA [63] and scanorama [69] were all sensitive to batch definitions. DESC was then applied to human pancreas datasets to test its ability to remove batch effects from multiple scRNA-seq platforms and yielded the highest ARI among the comparing approaches mentioned above. When applied to human PBMC data with interferon-beta stimulation, where biological variations are compounded by batch effect, DESC was shown to be the best in removing batch effect while preserving biological variations. DESC was also shown to remove batch effect for the monocytes and mouse bone marrow data, and DESC was shown to preserve the pseudotemporal structure. Finally, DESC scales linearly with the number of cells, and its running time is not affected by the increasing number of batches.

iMAP: Integration of Multiple single-cell datasets by Adversarial Paired-style transfer networks

iMAP [70] combines AE (Figures 2B and 4B) and GAN (Figures 2C and 4E) for batch effect removal. It is designed to remove batch biases while preserving dataset-specific biological variations.

Model

iMAP consists of two processing stages, each including a separate DL model. In the first stage, a special AE, whose decoder combines the output of two separate decoders $D_{\boldsymbol{\theta}_1}$ and $D_{\boldsymbol{\theta}_2}$, is trained such that

$$\mathbf{z}_n = E_{\boldsymbol{\phi}}(\mathbf{x}_n)\,;\hat{\mathbf{x}}_n = D_{\boldsymbol{\theta}}(\mathbf{z}_n, s_n) = \mathrm{ReLu}(D_{\boldsymbol{\theta}_1}(s_n) + D_{\boldsymbol{\theta}_2}(\mathbf{z}_n, s_n)) \tag{21}$$

where s_n is the one-hot encoded batch number of cell n. $D_{\boldsymbol{\theta}_1}$ can be understood as decoding the batch noise, whereas $D_{\boldsymbol{\theta}_2}$ reconstructs batch-removed expression from the latent variable $\mathbf{z}_n$. The training minimizes the loss in Eq. (19) except the 2nd loss is the content loss

$$L_t(\boldsymbol{\Theta}) = \sum_{n=1}^{N} \left\| \mathbf{z}_n - E_{\boldsymbol{\phi}}\left(D_{\boldsymbol{\theta}}\left(\mathbf{z}_n, \tilde{s}_n\right)\right)\right\|_2^2, \tag{22}$$

where $\tilde{s}_n$ is a random batch number. Minimizing $L_t(\boldsymbol{\Theta})$ further ensures that the reconstructed expression $\hat{\mathbf{x}}_n$ would be batch agnostic and has the same content as $\mathbf{x}_n$.

However, due to the limitation of AE, this step is still insufficient for batch removal. Therefore, a second stage is included to apply a GAN model to make expression distributions of the shared cell type across different baches indistinguishable. To identified the shared cell types, an MNNs strategy adapted from [32] was developed to identify MNN pairs across batches using batch effect independent $\mathbf{z}_n$ as opposed to $\mathbf{x}_n$. Then, a mapping generator $G_{\boldsymbol{\theta}_G}$ is trained using MNN pairs based on GAN such that $\mathbf{x}_n^{(A)} = G_{\boldsymbol{\theta}_G}(\mathbf{x}_n^{(S)})$, where $\mathbf{x}_n^{(S)}$ and $\mathbf{x}_n^{(A)}$ are the MNN pairs from batch S and an anchor batch A. The WGAN-GP loss as in Eq. (9) was adopted for the GAN training. After training, $G_{\boldsymbol{\theta}_G}$ is applied to all cells of a batch to generate batch-corrected expression.

Results

iMAP was first tested on benchmark datasets from human dendritic cells and Jurkat and 293 T cell lines

Table 7. Large single-cell data source used by various algorithms

Title	Sources	Notes
10× Single-cell gene expression dataset	https://support.10xgenomics.com/single-cell-gene-expression/datasets	Contains large collection of scRNA-seq dataset generated using 10× system
Tabula Muris	https://tabula-muris.ds.czbiohub.org/	Compendium of scRNA-seq data from mouse
HCA	https://data.humancellatlas.org/	Human single-cell atlas
MCA	https://figshare.com/s/865e694ad06d5857db4b, or GSE108097	Mouse single-cell atlas
scQuery	https://scquery.cs.cmu.edu/	A web server cell-type matching and key gene visualization. It is also a source for scRNA-seq collection (processed with common pipeline)
SeuratData	https://github.com/satijalab/seurat-data	List of datasets, including PBMC and human pancreatic islet cells
cytoBank	https://cytobank.org/	Community of big data cytometry

and then human pancreas datasets from five different platforms. All the datasets contain both batch-specific cells and batch-shared cell types. iMAP was shown to separate the batch-specific cell types but mix batch shared cell types and outperformed nine other existing batch correction methods including Harmony, scVI, fastMNN, Seurat, etc. iMAP was then applied to the large-scale Tabula Muris datasets containing over 100 K cells sequenced from two platforms. iMAP could not only reliably integrate cells from the same tissues but identify cells from platform-specific tissues. Finally, iMAP was applied to datasets of tumor-infiltrating immune cells and shown to reduce the dropout ratio and the percentage of ribosomal genes and non-coding RNAs, thus improving the detection of rare cell types and ligand-receptor interactions. iMAP scales with the number of cells, showing minimal time cost increase after the number of cells exceeds thousands. Its performance is also robust against model hyperparameters.

Dimensionality reduction, latent representation, clustering and data augmentation

Dimensionality reduction is indispensable for many type of scRNA-seq data analysis, considering the limited number of cell types in each biospecimen. Furthermore, biological processes of interests often involve the complex coordination of many genes, therefore, latent representations which capture biological variation in reduced dimensions are useful in interpreting experiment conditions and cell heterogeneity. Both AE- and VAE-based are capable of learning latent representations. VAE-based models have the benefit of regularity of the latent space and generative factors. The GAN-based models can produce augmented data that may in return to enhance the clustering, e.g. due to low representation of certain cell types.

Dimensionality reduction by AEs with gene-interaction constrained architecture

This study [71] considers AEs (Figures 2B and 4B) for learning the low-dimensional representation and specifically explores the benefit of incorporating prior biological knowledge of gene–gene interactions to regularize the AE network architecture.

Model

Several AE models with single or two hidden layers that incorporate gene interactions reflecting transcription factor (TF) regulations and protein–protein interactions (PPIs) are implemented. The models take normalized, log-transformed expressions and follow the general AE structure, including dimension-reducing and reconstructing layers, but the network architectures are not symmetrical. Specifically, gene interactions are incorporated such that each node of the first hidden layer represented a TF or a protein in the PPI; only genes that are targeted by TFs or involved in the PPI were connected to the node. Thus, the corresponding weights of $E_{\boldsymbol{\phi}}$ and $D_{\boldsymbol{\theta}}$ are set to be trainable and otherwise fixed at zero throughout the training process. Both unsupervised (AE-like) and supervised (cell-type label) learning were studied.

Results

Regularizing encoder connections with TF and PPI information considerably reduced the model complexity by almost 90% (7.5–7.6 M to 1.0–1.1 M). The clusters formed on the data representations learned from the models with or without TF and PPI information were compared with those from PCA, NMF, ICA, *t*-SNE and SIMLR [44]. The model with TF/PPI information and two hidden layers achieved the best performance by five of the six measures and the best average performance. In terms of the cell-type retrieval of single cells, the encoder models with and without TF/PPI information achieved the best performance in four and three cell types, respectively. PCA yielded the best performance in only two cell types. The DNN model with TF/PPI information and two hidden layers again achieved the best average performance across all cell types. In summary, this study demonstrated a biologically meaningful way to regularize AEs by the prior biological knowledge for learning the representation of scRNA-seq data for cell clustering and retrieval.

Table 8. Evaluation metrics used in surveyed DL algorithms

Evaluation Method	Equations	Explanation
Pseudobulk RNA-seq		Average of normalized (log2-transformed) scRNA-seq counts across cells is calculated and then correlation coefficient between the pseudobulk and the actual bulk RNA-seq profile of the same cell type is evaluated.
Mean squared error (MSE)	$\mathrm{MSE} = \frac{1}{n}\sum_{i=1}^{n}(x_i - \hat{x}_i)^2$	MSE assesses the quality of a predictor, or an estimator, from a collection of observed data x, with $\hat{x}$ being the predicted values.
Pearson correlation	$\rho_{X,Y} = \frac{cov(X,Y)}{\sigma_X \sigma_Y}$	where cov() is the covariance, σ_X and σ_Y are the standard deviation of X and Y, respectively.
Spearman correlation	$\rho_s = \rho_{r_X,r_Y} = \frac{cov(r_X,r_Y)}{\sigma_{r_X}\sigma_{r_Y}}$	The Spearman correlation coefficient is defined as the Pearson correlation coefficient between the rank variables, where r_X is the rank of X.
Entropy of accuracy, H_{acc} [21]	$H_{\mathbf{acc}} = -\frac{1}{M}\sum_{i=1}^{M}\sum_{j=1}^{N_i} p_i(x_j)\log(p_i(x_j))$	Measures the diversity of the ground-truth labels within each predicted cluster group. $p_i(x_j)$ (or $q_i(x_j)$) are the proportions of cells in the jth ground-truth cluster (or predicted cluster) relative to the total number of cells in the ith predicted cluster (or ground-truth clusters), respectively.
Entropy of purity, H_{pur} [21]	$H_{\mathbf{pur}} = -\frac{1}{N}\sum_{i=1}^{N}\sum_{j=1}^{M_i} q_i(x_j)\log(q_i(x_j))$	Measures the diversity of the predicted cluster labels within each ground-truth group.
Entropy of mixing [32]	$E = \sum_{i=1}^{C} p_i \log(p_i)$	This metric evaluates the mixing of cells from different batches in the neighborhood of each cell. C is the number of batches, and p_i is the proportion of cells from batch i among N nearest cells.
MI [162]	$\mathbf{MI}(U,V) = \sum_{i=1}^{\lvert U\rvert}\sum_{j=1}^{\lvert V\rvert} P_{UV}(i,j)\log(\frac{P_{UV}(i,j)}{P_U(i)P_V(j)})$	where $P_U(i) = \frac{\lvert U_i\rvert}{N}$ and $P_V(j) = \frac{\lvert V_j\rvert}{N}$. Also, define the joint distribution probability is $P_{UV}(i,j) = \frac{\lvert U_i \cap V_j\rvert}{N}$. The MI is a measure of mutual dependency between two cluster assignments U and V.
Normalized MI (NMI) [163]	$\mathbf{NMI}(U,V) = \frac{2\times\mathbf{MI}(U,V)}{[H(U)+H(V)]}$	where $H(U) = \sum P_U(i)\log(P_U(i)), H(V) = \sum P_V(i)\log(P_V(i))$. The NMI is a normalization of the MI score between 0 and 1.
KL divergence [164]	$D_{\mathbf{KL}}(P \mid \lvert Q) = \sum_{x\in\chi} P(x)\log(\frac{P(x)}{Q(x)})$	where discrete probability distributions P and Q are defined on the same probability space χ. This relative entropy is the measure for directed divergence between two distributions.
Jaccard Index	$J(U,V) = \frac{\lfloor U\cap V\rfloor}{\lfloor U\cup V\rfloor}$	$0 \le J(U,V) \le 1$. $J = 1$ if clusters U and V are the same. If U are V are empty, J is defined as 1.
Fowlkes–Mallows Index for two clustering algorithms (FM)	$\mathrm{FM} = \sqrt{\frac{\mathrm{TP}}{\mathrm{TP+FP}} \times \frac{\mathrm{TP}}{\mathrm{TP+FN}}}$	TP as the number of pairs of points that are present in the same cluster in both U and V; FP as the number of pairs of points that are present in the same cluster in U but not in V; FN as the number of pairs of points that are present in the same cluster in V but not in U and TN as the number of pairs of points that are in different clusters in both U and V.
Rand index (RI)	$\mathrm{RI} = (a+b)/\binom{n}{2}$	Measure of constancy between two clustering outcomes, where a (or b) is the count of pairs of cells in one cluster (or different clusters) from one clustering algorithm but also fall in the same cluster (or different clusters) from the other clustering algorithm.
Adjusted Rand index (ARI) [165]	$\mathrm{ARI} = \frac{\mathrm{RI}-E[\mathrm{RI}]}{\max(\mathrm{RI})-E[\mathrm{RI}]}$	ARI is a corrected-for-chance version of RI, where E[RI] is the expected RI.
Silhouette index	$s(i) = \frac{b(i)-a(i)}{\max(a(i),b(i))}$	where $a(i)$ is the average dissimilarity of ith cell to all other cells in the same cluster, and $b(i)$ is the average dissimilarity of ith cell to all cells in the closest cluster. The range of $s(i)$ is $[-1,1]$, with 1 to be well-clustered and -1 to be completely misclassified.
MMD [64]	$\mathbf{MMD}(F,p,q) = \sup_{f\in F}\lVert\mu_p - \mu_q\rVert_f$	MMD is a non-parametric distance between distributions based on the reproducing kernel Hilbert space, or, a distance-based measure between two distribution p and q based on the mean embeddings μ_p and μ_q in a reproducing kernel Hilbert space F.

(*Continued*)

Table 8. Continued

Evaluation Method	Equations	Explanation
kBET [166]	$a_n^k = \sum_{l=1}^{L} \frac{\left(N_{nl}^k - k \bullet f_l\right)^2}{k \bullet f_l} \sim X_{L-1}^2$	Given a dataset of N cells from L batches with N_l denoting the number of cells in batch l, N_{nl}^k is the number of cells from batch l in the KNN s of cell n, f_l is the global fraction of cells in batch l, or $f_l = \frac{N_l}{N}$, and X_{L-1}^2 denotes the X^2 distribution with $L-1$ degrees of freedom. It uses a X^2-based test for random neighborhoods of fixed size to determine the significance ('well-mixed').
LISI [34]	$\frac{1}{\lambda(n)} = \frac{1}{\Sigma_{l=1}^{L}(p(l))^2}$	This is the inverse Simpson's Index in the KNNs of cell n for all batches, where $p(l)$ denotes the proportion of batch l in the KNNs. The score reports the effective number of batches in the KNNs of cell n.
Homogeneity	$\mathrm{HS} = 1 - \frac{H(P(U\|V))}{H(P(U))}$	where $H()$ is the entropy, and U is the ground-truth assignment and V is the predicted assignment. The HS range from 0 to 1, where 1 indicates perfectly homogeneous labeling.
Completeness	$\mathrm{CS} = 1 - \frac{H(P(V\|U))}{H(P(V))}$	Its values range from 0 to 1, where 1 indicates all members from a ground-truth label are assigned to a single cluster.
V-Measure [167]	$V_\beta = \frac{(1+\beta)\mathrm{HS} \times \mathrm{CS}}{\beta \mathrm{HC} + \mathrm{CS}}$	where β indicates the weight of HS. V-Measure is symmetric, i.e. switching the true and predicted cluster labels does not change V-Measure.
Precision, recall	$\text{Precision} = \frac{\mathrm{TP}}{\mathrm{TP}+\mathrm{FP}}$, $\text{recall} = \frac{\mathrm{TP}}{\mathrm{TP}+\mathrm{FN}}$	TP: true positive, FP: false positive, FN, false negative.
Accuracy	$\text{Accuracy} = \frac{\mathrm{TP}+\mathrm{TN}}{\mathrm{N}}$	N: all samples tested, TN: true negative
F_1-score	$F_1 = \frac{2\ \text{Precision} \bullet \text{Recall}}{\text{Precision} + \text{Recall}}$	A harmonic mean of precision and recall. It can be extended to F_β where β is a weight between precision and recall (similar to V-measure).
AUC, RUROC	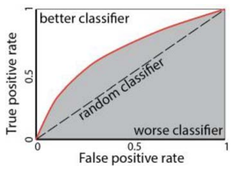	Area Under Curve (grey area). Receiver operating characteristic (ROC) curve (red line). A similar measure can be performed on the Precision-Recall curve (PRC) or AUPRC. PRCs summarize the trade-off between the true positive rate and the positive predictive value for a predictive model (mostly for an imbalanced dataset).

Dhaka: A VAE-based dimension reduction model

Dhaka [72] was proposed to reduce the dimension of scRNA-seq data for efficient stratification of tumor subpopulations.

Model

Dhaka adopts a general VAE formulation (Figures 2A and 4C). It takes the normalized, log-transformed expressions of a cell as input and outputs the low-dimensional representation.

Result

Dhaka was first tested on the simulated dataset. The simulated dataset contains 500 cells, each including 3 K genes, clustered into 5 different clusters with 100 cells each. The clustering performance was compared with other methods including t-SNE, PCA, SIMLR, NMF, an AE, MAGIC and scVI. Dhaka was shown to have an ARI higher than most other comparing methods. Dhaka was then applied to the Oligodendroglioma data and could separate malignant cells from non-malignant microglia/macrophage cells. It also uncovered the shared glial lineage and differentially expressed genes for the lineages. Dhaka was also applied to the Glioblastoma data and revealed an evolutionary trajectory of the malignant cells where cells gradually evolve from a stemlike state to a more differentiated state. In contrast, other methods failed to capture this underlying structure. Dhaka was next applied to the Melanoma cancer dataset [73] and uncovered two distinct clusters that showed the intra-tumor heterogeneity of the Melanoma samples. Dhaka was finally applied to copy number variation data [74] and shown to identify one major and one minor cell clusters, of which other methods could not find.

scvis: A VAE for capturing low-dimensional structures

scvis [75] is a VAE network (Figures 2A and 4C) that learns that the low-dimensional representations capture both local and global neighboring structures in scRNA-seq data.

Model

scvis adopts the generic VAE formulation described in section 3.1. However, it has a unique loss function defined as

$$L(\boldsymbol{\Theta}) = -\mathcal{L}(\boldsymbol{\Theta}) + \lambda L_t(\boldsymbol{\Theta}), \tag{23}$$

where $\mathcal{L}(\boldsymbol{\Theta})$ is ELBO as in Eq. (3) and L_t is a regularizer using non-symmetrized t-SNE objective function [75], which is defined as

$$L_t(\boldsymbol{\Theta}) = \sum_{i=1}^{N}\sum_{j=1,j\neq i}^{N} p_{j|i} \log \frac{p_{j|i}}{q_{j|i}}, \quad (24)$$

where i and j are two different cells, $p_{i|j}$ measures the local cell relationship in the data space and $q_{j|i}$ measures such relationship in the latent space. Because t-SNE algorithm preserves the local structure of high dimensional space, L_t learns local structures of cells.

Results

scvis was tested on the simulated data and outperformed t-SNE in a nine-dimensional space task. scvis preserved both local structure and global structure. The relative positions of all clusters were well kept but outliers were scattered around clusters. Using simulated data and comparing to t-SNE, scvis generally produced consistent and better patterns among different runs, while t-SNE could not. scvis also presented good results on adding new data to an existing embedding, with median accuracy on new data at 98.1% for $K=5$ and 94.8% for $K=65$, when train K cluster on original data then test the classifier on new-generated sample points. The scvis was subsequently tested on four real datasets including metastatic melanoma, oligodendroglioma, mouse bipolar and mouse retina datasets. In each dataset, scvis was showed to preserve both the global and local structure of the data.

scVAE: VAE for single-cell gene expression data

scVAE [76] includes multiple VAE models (Figures 2A and 4C) for denoising gene expression levels and learning the low-dimensional latent representation of cells. It investigates different choices of the likelihood functions in the VAE model to model different data sets.

Model

scVAE is a conventional fully connected network. However, different distributions have been discussed for $p(x_{gn}|\ \nu_{gn}, \alpha_{gn})$ to model different data behaviors. Specifically, scVAE considers Poisson, constrained Poisson and negative binomial distributions for count data, piece-wise categorical Poisson for data including both high and low counts, and zero-inflated version of these distributions to model missing values. To model multiple modes in cell expressions, a Gaussian mixture is also considered for $q(\mathbf{z}_n|\mathbf{x}_n, s_n)$, resulting in a GMVAE. The inference process still follows that of a VAE as discussed in section 3.1.

Results

scVAEs were evaluated on the PBMC data and compared with factor analysis (FA) models. The results showed that GMVAE with negative binomial distribution achieved the highest lower bound and ARI. Zero-inflated Poisson distribution performed the second best. All scVAE models outperformed the baseline linear FA model, which suggested that a non-linear model is needed to capture single-cell genomic features. GMVAE was also compared with Seurat and shown to perform better using the withheld data. However, scVAE performed no better than scVI [17] or scvis [75], both are VAE models.

VASC: VAE for scRNA-seq

VASC [77] is another VAE (Figures 2A and 4C) for dimension reduction and latent representation but it models dropout.

Model

VASC's input is the log-transformed expression but rescaled in the range [0,1]. A dropout layer (dropout rate of 0.5) is added after the input layer to force subsequent layers to learn to avoid dropout noise. The encoder network has three layers fully connected and the first layer uses linear activation, which acts like an embedded PCA transformation. The next two layers use the ReLU activation, which ensures a sparse and stable output. This model's novelty is the zero-inflation layer (ZI layer), which is added after the decoder to model scRNA-seq dropout events. The probability of dropout event is defined as $e^{-\hat{x}^2}$ where $\hat{x}$ is the recovered expression value obtained by the decoder network. Since back-propagation cannot deal with a stochastic network with categorical variables, a Gumbel-softmax distribution [78] is introduced to address the difficulty of the ZI layer. The loss function of the model takes the form $L = \mathcal{L}(\boldsymbol{\Theta}) + \lambda L_{\mathrm{KL}}(\boldsymbol{\Theta})$, where $\mathcal{L}$ is the binary entropy because the input is scaled to [0 1], and L_{KL} a loss performed using Kullback–Leibler (KL) divergence on the latent variables. After the model is trained, the latent code can be used as the dimension-reduced feature for downstream tasks and visualization.

Results

VASC was compared with PCA, t-SNE, ZIFA and SIMLR on 20 datasets. In the study of embryonic development from zygote to blast cells, all methods roughly re-established the development stages of different cell types in the dimension-reduced space. However, VASC showed the better performance to model embryo developmental progression. In the Goolam, Biase and Yan datasets, scRNA-seq data were generated through embryonic development stages from zygote to blast, VASC re-established development stage from 1, 2, 4, 8, 16 to blast, while other methods failed. In the Pollen, Kolodziejczyk and Baron datasets, VASC formed an appropriate cluster, either with homogeneous cell type, preserved proper relative positions, or minimal batch influence. Interestingly, when tested on the PBMC dataset, VASC was shown to identify the major global structure (B cells, CD4+, CD8+ T cells, NK cells, Dendritic cells) and detect subtle differences within monocytes (FCGR3A+ versus CD14+ monocytes), indicating the capability of VASC handling a large number of cells or cell types. Quantitative clustering performance in NMI, ARI, homogeneity and completeness was also performed. VASC always ranked top two in all the datasets. In terms of NMI and ARI, VASC best performed on 15 and 17 out of 20 datasets, respectively.

scDeepCluster

scDeepCluster [79] is an AE network (Figures 2B and 4B) that simultaneously learns feature representation and performs clustering via explicit modeling of cell clusters as in DESC.

Model

Similar to DCA, scDeepCluster adopts a ZINB distribution for $\boldsymbol{x}_n$ as in Eqs. (13) and (15). The loss is similar to Eq. (19) except that the first term is the negative log-likelihood of the ZINB data distribution as defined in Eq. (15) and the second L_c is a clustering loss performed using KL divergence as in DESC algorithm. Compared with ***csvis, scDeepcluster focuses more on clustering assignment due to the KL divergence.

Results

scDeepCluster was first tested on the simulation data and compared with other seven methods including DCA [18], two multi-kernel spectral clustering methods MPSSC [80] and SIMLR [44], CIDR [61], PCA + k-mean, scvis [75] and DEC [81]. In different dropout rate simulations, scDeepCluster significantly outperformed the other methods consistently. In signal strength, imbalanced sample size and scalability simulations, scDeepcluster outperformed all other algorithms and scDeepCluster and most notably advantages for weak signals, robust against different data imbalance levels and scaled linearly with the number of cells. scDeepCluster was then tested on four real datasets (10X PBMC, Mouse ES cells, Mouse bladder cells, Worm neuron cells) and shown to outperform all other comparing algorithms. Particularly, MPSSC and SIMLR failed to process the full datasets due to quadratic complexity.

cscGAN: Conditional single-cell generative adversarial neural networks

cscGAN [82] is a GAN model (Figures 2C and 4E) designed to augment the existing scRNA-seq samples by generating expression profiles of specific cell types or subpopulations.

Model

Two models, csGAN and cscGAN, were developed following the general formulation of WGAN described in section 3.3. The difference between the two models is that cscGAN is a conditional GAN such that the input to the generator also includes a class label y or cell type, i.e. $\boldsymbol{\phi}_G(\mathbf{z}, y)$. The projection-based conditioning (PCGAN) method [83] was adopted to obtain the conditional GAN. For both models, the generator (three layers of 1024, 512 and 256 neurons) and discriminator (three layers of 256, 512 and 1024 neurons) are fully connected DNNs.

Results

The performance of scGAN was first evaluated using PBMC data. The generated samples were shown to capture the desired clusters and the real data's regulons. Additionally, the AUC performance for classifying real from generated samples by a Random Forest classifier only reached 0.65, performance close to 0.5. Finally, scGAN's generated samples had a smaller MMD than those of Splatter, a state-of-the-art scRNA-seq data simulator [84]. Even though a large MMD was observed for scGAN when compared with that of SUGAR, another scRNA-seq simulator, SUGAR [85] was noted for prohibitively high runtime and memory. scGAN was further trained and assessed on the bigger mouse brain data and shown to model the expression dynamics across tissues. Then, the performance of cscGAN for generating cell-type-specific samples was evaluated using the PBMC data. cscGAN was shown to generate high-quality scRAN-seq data for specific cell types. Finally, the real PBMC samples were augmented with the generated samples. This augmentation improved the identification of rare cell types and the ability to capture transitional cell states from trajectory analysis.

Multi-functional models

Given the versatility of AE and VAE in addressing different scRAN-seq analysis challenges, DL models possessing multiple analysis functions have been developed. We survey these models in this section.

scVI: Single-cell variational inference

scVI [17] is designed to address a range of fundamental analysis tasks, including batch correction, visualization, clustering and differential expression.

Model

scVI is a VAE (Figures 2A and 4C) that models the counts of each cell from different batches. scVI adopts a ZINB distribution for x_{gn}

$$p\left(x_{gn}|\pi_{gn}, L_n, \nu_{gn}, \alpha\right) = \pi_{gn}\delta(0) + \left(1-\pi_{gn}\right) NB\left(L_n\nu_{gn}, \alpha_g\right), \tag{25}$$

which is defined similarly as Eq. (14) in DCA, except that L_n denotes the scaling factor for cell n, which follows a log-Normal ($log\mathcal{N}$) prior as $p(L_n) = log\mathcal{N}(\mu_{L_n}, \sigma^2_{L_n})$; therefore, ν_{gn} represents the mean counts normalized by L_n. Now, let $s_n \in \{0,1\}^B$ be the batch ID of cell n with B being the total number of batches. Then, ν_{gn} and π_g are further modeled as functions of the d-dimension latent variable $\mathbf{z}_n \in \mathbb{R}^d$ and the batch ID s_n by the decoder networks $D_{\boldsymbol{\theta}_\nu}$ and $D_{\boldsymbol{\theta}_\pi}$ as

$$\boldsymbol{\nu}_n = D_{\boldsymbol{\theta}_\nu}\left(\mathbf{z}_n, s_n\right), \boldsymbol{\pi}_n = D_{\boldsymbol{\theta}_\pi}\left(\mathbf{z}_n, s_n\right), \tag{26}$$

where the gth element of $\boldsymbol{\nu}_n$ and $\boldsymbol{\pi}_n$ are ν_{gn} and π_g, respectively, and $\boldsymbol{\theta}_\nu$ and $\boldsymbol{\theta}_\pi$ are the decoder weights. Note that the lower layers of the two decoders are shared. For inference, both $\mathbf{z}_n$ and L_n are considered as latent variables, and therefore, $q(x_n, s_n) = q(\mathbf{z}_n|\mathbf{x}_n, s_n)q(L_n|\mathbf{x}_n, s_n)$ is a mean-field approximate to the intractable posterior distribution $p(\mathbf{z}_n, L_n|\mathbf{x}_n, s_n)$ and

$$\begin{aligned} q\left(z_n|x_n, s_n\right) &= \mathcal{N}\left(\mu_{zn}, diag\left(\sigma^2_{Zn}\right)\right), \\ q\left(L_n|x_n, s_n\right) &= log\,\mathcal{N}\left(\mu_{Ln}, diag\left(\sigma^2_{Ln}\right)\right), \end{aligned} \quad (27)$$

whose means and variances $\{\boldsymbol{\mu}_{zn}, \boldsymbol{\sigma}^2_{Zn}\}$ and $\{\boldsymbol{\mu}_{Ln}, \boldsymbol{\sigma}^2_{Ln}\}$ are defined by the encoder networks E_Z and E_L applied to $\mathbf{x}_n$ and s_n as

$$\begin{aligned} \left\{\mu_{zn}, \sigma^2_{Zn}\right\} &= E_{\phi_Z}\left(x_n, s_n\right), \\ \left\{\mu_{Ln}, \sigma^2_{Ln}\right\} &= E_{\phi_L}\left(z_n, s_n\right) \end{aligned} \quad (28)$$

where $\boldsymbol{\phi}_z$ and $\boldsymbol{\phi}_L$ are the encoder weights. Note that, like the decoders, the lower layers of the two encoders are also shared. Overall, the model parameters to be estimated by the variational optimization is $\boldsymbol{\Theta} = \{\boldsymbol{\theta}_\nu, \boldsymbol{\theta}_\pi, \boldsymbol{\phi}_z, \boldsymbol{\phi}_L, \alpha_g\}$. After inference, $\mathbf{z}_n$ are used for visualization and clustering; ν_{gn} provides a batch-corrected, size-factor normalized estimate of gene expression for each gene g in each cell n. An added advantage of the probabilistic representation by scVI is that it provides a natural probabilistic treatment of the subsequent differential analysis, resulting in lower variance in the adopted hypothesis tests.

Results

scVI was evaluated for its scalability, the performance of imputation. For scalability, ScVI was shown to be faster than most non-DL algorithms and scalable to handle twice as many cells as non-DL algorithms with a fixed memory. For imputation, ScVI, together with other ZINB-based models, performed better than methods using alternative distributions. However, it underperformed for the dataset (HEMATO) with fewer cells. For the latent space, scVI was shown to provide a comparable stratification of cells into previously annotated cell types. Although scVI failed to ravel SIMLR, it is among the best in capturing biological structures (hierarchical structure, dynamics, etc.) and recognizing noise in data. For batch correction, it outperforms ComBat. For normalizing sequencing depth, the size factor inferred by scVI was shown to be strongly correlated with the sequencing depth. Interestingly, the negative binomial distribution in the ZINB was found to explain the proportions of zero expressions in the cells, whereas the zero probability π_{gn} is found to be more correlated with alignment errors. For differential expression analysis, scVI was shown to be among the best.

LDVAE: Linearly decoded VAE

LDVAE [86] is an adaption of scVI to improve the model interpretability but it still benefits from the scalability and efficiency of scVI. Also, this formulation applies to general VAE models and thus is not restricted to scRNA-seq analysis.

Model

LDVAE follows scVI's formulation but replaces the decoder $D_{\boldsymbol{\theta}_\nu}$ in Eq. (26) by a linear model

$$\boldsymbol{\nu}_n = \mathbf{W}\mathbf{z}_n, \quad (29)$$

where $\mathbf{W} \in \mathbb{R}^{d \times G}$ is the weight matrix. Being the linear decoder provides interpretability in the sense that the relationship between latent representation $\mathbf{z}_n$ and gene expression $\boldsymbol{\nu}_n$ can be readily identified. LDVAE still follows the same loss and non-linear inference scheme as scVI.

Results

LDVAE's latent variable $\mathbf{z}_n$ could be used for clustering of cells with similar accuracy as a VAE. Although LDVAE had a higher reconstruction error than VAE, due to the linear decoder, the variations along the different axes of $\mathbf{z}_n$ establish direct linear relationships with input genes. As an example from analyzing mouse embryo scRNA-seq, $z_{1,n}$, the second element of $\mathbf{z}_n$, is shown to relate to simultaneous variations in the expression of gene *Pou5f1* and *Tdgf1*. In contrast, such interpretability would be intractable without approximation for a VAE. LDVAE was also shown to induce fewer correlations between latent variables and to improve the grouping of the regulatory programs. LDVAE is capable to scale to a large dataset with ∼2 M cells.

SAUCIE

SAUCIE [15] is an AE (Figures 2B and 4B) designed to perform multiple functions, including clustering, batch correlation, imputation and visualization. SAUCIE is applied to the normalized data instead of count data.

Model

SAUCIE includes multiple model components designed for different functions.

(i) Clustering: SAUCIE first introduced a 'digital' binary encoding layer $\boldsymbol{h}^c \in \{0,1\}^J$ in the decoder D that functions to encode the cluster ID. To learn this encoding, an entropy loss is introduced

$$L_D = \sum\nolimits_{k=1}^{K} p_k \, \log p_k, \quad (30)$$

where p_k is the probability (proportion) of activation on neuron k by the previous layer. Minimizing this entropy loss promotes sparse neurons, thus forcing a binary encoding. To encourage clustering behavior, SAUCIE also introduced an intracluster loss as

$$L_C = \sum_{i,j:h^c_i = h^c_j} \left\|\hat{\mathbf{x}}_i - \hat{\mathbf{x}}_j\right\|^2, \quad (31)$$

which computes the distance L_C between the expressions of a pair of cells $(\hat{\mathbf{x}}_i, \hat{\mathbf{x}}_j)$ that have the same cluster ID $(h^c_i = h^c_j)$.

(ii) Batch correction: To correct the batch effect, an MMD loss is introduced to measure the differences in terms of the distribution between batches in the latent space

$$L_B = \sum_{l=1, l\neq ref}^{B} \mathrm{MMD}\left(\mathbf{z}_{\mathbf{ref}}, \mathbf{z}_l\right), \tag{32}$$

where B is the total number of batches and $\mathbf{z}_{\mathbf{ref}}$ is the latent variable of an arbitrarily chosen reference batch.

(iii) Imputation and visualization: The output of the decoder is taken by SAUCIE as an imputed version of the input gene expression. To visualize the data without performing an additional dimension reduction directly, the dimension of the latent variable $\mathbf{z}_n$ is forced to 2.

Training the model includes two sequential runs. In the first run, an AE is trained to minimize the loss $L_0 + \lambda_B L_B$ with L_0 being the MSE reconstruction loss defined in Eq. (9) so that a batch-corrected, imputed input $\widetilde{\boldsymbol{x}}$ can be obtained at the output of the decoder. In the second run, the bottleneck layer of the encoder from the first run is replaced by a 2D latent code for visualization and a digital encoding layer is also introduced. This model takes the cleaned $\widetilde{\boldsymbol{x}}$ as the input and is trained for clustering by minimizing the loss $L_0 + \lambda_D L_D + \lambda_C L_C$. After the model is trained, $\widetilde{x}$ is the imputed, batch-corrected gene expression. The 2D latent code is used for visualization and the binary encoder encodes the cluster ID.

Results

SAUCIE was evaluated for clustering, batch correction, imputation and visualization on both simulated and real scRNA-seq and scCyToF datasets. The performance was compared with minibatch *kmeans*, Phenograph [87] and 22 for clustering; MNN [32] and CCA [33] for batch correction; PCA, Monocle2 [88], diffusion maps, UMAP [89], *t*-SNE [90] and PHATE [91] for visualization; and MAGIC [57], scImpute [37] and nearest neighbors completion (NN completion) for imputation. Results showed that SAUCIE had a better or comparable performance with other approaches. Also, SAUCIE has better scalability and faster runtimes than any of the other models. SAUCIE's results on the scCyToF dengue dataset were further analyzed in greater detail. SAUCIE was able to identify subtypes of the T cell populations and demonstrated distinct cell manifold between acute and healthy subjects.

scScope

scScope [92] is an AE (Figures 2B and 4D) with recurrent steps designed for imputation and batch correction.

Model

scScope has the following model design for batch correction and imputation.

(i) Batch correction: A batch correction layer is applied to the input expression as

$$\boldsymbol{x}_n^c = \mathrm{ReLu}\left(\boldsymbol{x}_n - \boldsymbol{B}\boldsymbol{u}_c\right), \tag{33}$$

where **ReLU** is the ReLu activation function, $\boldsymbol{B} \in \mathbb{R}^{G\times K}$ is the batch correction matrix, $\boldsymbol{u}_c \in \{0,1\}^{K\times \mathbf{1}}$ is an indicator vector with entry 1 indicates the batch of the input and K is the total number of batches.

(ii) Recursive imputation: Instead of using the reconstructed expression $\hat{\boldsymbol{x}}_n$ as the imputed expression like in SAUCIE, scScope adds an imputer to $\hat{\boldsymbol{x}}_n$ to recursively improve the imputation result. The imputer is a single-layer AE, whose decoder performs the imputation as

$$\hat{\hat{\boldsymbol{x}}}_n = P_I\left[D_I\left(\hat{\hat{\mathbf{z}}}_n\right)\right], \tag{34}$$

where $\hat{\hat{\mathbf{z}}}_n$ is the output of the imputer encoder, D_I is the imputer decoder and P_I is a masking function that sets the elements in $\hat{\hat{\boldsymbol{x}}}_n$ that corresponds to the non-missing values to zero. Then, $\hat{\hat{\boldsymbol{x}}}_n$ will be fed back to fill the missing value in the batch corrected input as $\boldsymbol{x}_n^c + \hat{\hat{\boldsymbol{x}}}_n$, which will be passed on to the main AE. This recursive imputation can iterate multiple cycles as selected.

The loss function is defined as

$$\mathcal{L}\left(\boldsymbol{\Theta}\right) = \sum_{n=1}^{N}\sum_{t=1}^{T}\left\|P_I^{-}\left[\boldsymbol{x}_n^c - \hat{\boldsymbol{x}}_n^t\right]\right\|^2, \tag{35}$$

where T is the total number of recursion, $\hat{\boldsymbol{x}}_n^t$ is the reconstructed expression at tth recursion, P_I^{-} is another masking function that forces the loss to compute only the non-missing values in $\boldsymbol{x}_n^c$.

Results

scScope was evaluated for its scalability, clustering, imputation and batch correction. It was compared with PCA, MAGIC, ZINB-WaVE, SIMLR, AE, scVI and DCA. For scalability and training speed, scScope was shown to offer scalability (for >100 K cells) with high efficiency (faster than most of the approaches). For clustering results, scScope outperformed most of the algorithms on small simulated datasets but offered similar performance on large simulated datasets. For batch correction, scScope performed comparably with other approaches but with faster runtime. For imputation, scScope produced smaller errors consistently across a different range of expression. scScope was further shown to be able to identify rear cell populations from a large mix of cells.

Automated cell-type identification

scRNA-seq can catalog cell types in complex tissues under different conditions. However, the commonly adopted manual cell typing approach based on known markers is time-consuming and less reproducible. We survey DL models of automated cell-type identification.

DigitalDLSorter

DigitalDLSorter [51] was proposed to identify and quantify the immune cells infiltrated in tumors captured in bulk RNA-seq, utilizing single-cell RNA-seq data.

Model

DigitalDLSorter is a 4-layer DNN (Figure 4A) (2 hidden layers of 200 neurons each and an output of 10 cell types). The DigitalDLSorter is trained with two single-cell datasets: breast cancers [93] and colorectal cancers [94]. For each cell, it is determined to be tumor cell or non-tumor cell using RNA-seq based CNV method [93], followed by using xCell algorithm [95] to determine immune cell types for non-tumor cells. Different pseudo bulk (from 100 cells) RNA-seq datasets were prepared with known mixture proportions to train the DNN. The output of DigitalDLSorter is the predicted proportions of cell types in the input bulk sample.

Result

DigitalDLSorter was first tested on simulated bulk RNA-seq samples. DigitalDLSorter achieved excellent agreement (linear correlation of 0.99 for colorectal cancer, and good agreement in quadratic relationship for breast cancer) at predicting cell types proportion. The proportion of immune and non-immune cell subtypes of test bulk TCGA samples was predicted by DigitalDLSorter and the results showed a very good correlation to other deconvolution tools including TIMER [93], ESTIMATE [96], EPIC [97] and MCPCounter [98]. Using DigitalDLSorter predicted CD8+ (good prognosis for overall and disease-free survival) and Monocytes-Macrophages (MM, indicator for protumoral activity) proportions, it is found that patients with higher CD8+/MM ratio had better survival for both cancer types than those with lower CD8+/MM ratio. Both EPIC and MCPCounter yielded non-significant survival associations using their cell proportion estimate.

scCapsNet

scCapsNet [52] is an interpretable capsule network designed for cell-type prediction. The paper showed that the trained network could be interpreted to inform marker genes and regulatory modules of cell types.

Model

scCapsNet takes log-transformed, normalized expressions as input and follows the general CapsNet model described in Section 3.4. Capsule $\boldsymbol{v}_k$ represents the probability of a single cell $\boldsymbol{x}_n$ belonging to cell type k, which will be used for cell-type classification. Once trained, the interpretation of marker genes and regulatory modules can be achieved by determining first the important primary capsules for each cell type and then the most significant genes for each important primary capsule (identified based on c_{kl} directly). To determine the genes that are important for an important primary capsule l, genes are ranked base on the scores of the first principal component computed from the columns of $\mathbf{W}_{P,l}$ in Eq. (15) and then the markers are obtained by a greedy search along with the ranked list for the best classification performance.

Results

scCapsNet's performance was evaluated on human PBMCs [99] and mouse retinal bipolar cells [100] datasets and shown to have comparable accuracies (99% and 97%, respectively) with DNN and other popular ML algorithms (SVM, random forest, LDA and nearest neighbor). However, the interpretability of scCapsNet was demonstrated extensively. First, examining the coupling coefficients for each cell type showed that only a few primary capsules have high values and thus are effective. Subsequently, a set of core genes were identified for each effective capsule using the greedy search on the PC-score ranked gene list. GO enrichment analysis showed that these core genes were enriched in cell-type-related biological functions. Mapping the expression data into space spanned by PCs of the columns of $\mathbf{W}_{P,l}$ corresponding to all core genes uncovered regulatory modules that would be missed by the t-SNE of gene expressions, which demonstrated the effectiveness of the embeddings learned by scCapsNet in capturing the functionally important features.

netAE: Network-enhanced AE

netAE [101] is a VAE-based semi-supervised cell-type prediction model (Figures 2A and 4C) that deals with scenarios of having a small number of labeled cells.

Model

netAE works with UMI counts and assumes a ZINB distribution for x_{gn} as in Eq. (25) in scVI. However, netAE adopts the general VAE loss as in Eq. (6) with two function-specific loss as

$$L(\boldsymbol{\Theta}) = -\mathcal{L}(\boldsymbol{\Theta}) + \lambda_1 \sum\nolimits_{n \in S} Q(\mathbf{z}_n) + \lambda_2 \sum\nolimits_{n \in S_L} log f(y_n|\mathbf{z}_n), \quad (36)$$

where S is a set of indices for all cells and S_L is a subset of S for only cells with cell-type labels, Q is modified Newman and Girvan modularity [102] that quantifies cluster strength using $\mathbf{z}_n$, f is the softmax function and y_n is the cell-type label. The second loss in Eq. (36) functions as a clustering constraint and the last term is the cross-entropy loss that constrains the cell-type classification.

Results

netAE was compared with popular dimension reduction methods including scVI, ZIFA, PCA and AE as well as a semi-supervised method scANVI [103]. For different dimensionality reduction methods, cell-type classification from latent features of cells was carried out using KNN and logistic regression. The effect of different labeled samples sizes on classification performance was also investigated, where the sample size varied from as few as 10 cells to 70% of all cells. Among 3 test datasets (mouse brain cortex, human embryo development and mouse hematopoietic stem and progenitor cells), netAE outperformed most of the baseline methods. Latent features were visualized using *t*-SNE and cell clusters by netAE were tighter than those by other embedding spaces. netAE also showed consistency of better cell-type classification with improved cell-type clustering. This suggested that the latent spaces learned with added modularity constraint in the loss helped identify clusters of similar cells. Ablation study by removing each of the three loss terms in Eq. (36) showed a drop of cell-type classification accuracy, suggesting that all three were necessary for the optimal performance.

scDGN: supervised adversarial alignment of single-cell RNA-seq data

scDGN [53], or Single Cell Domain Generalization Network (Figure 4G**)**, is a domain adversarial network that aims to accurately assign cell types of single cells while performing batch removal (domain adaptation) at the same time. It benefits from the superior ability of domain adversarial learning to learn representations that are invariant to technical confounders.

Model

scDGN takes the log-transformed, normalized expression as the input and has three main modules: (i) an encoder ($E_{\boldsymbol{\phi}}(\boldsymbol{x}_n)$) for dimension reduction of scRNA-seq data, (ii) cell-type classifier, $C_{\boldsymbol{\phi}_C}(E_{\boldsymbol{\phi}}(\boldsymbol{x}_n))$ with parameters $\boldsymbol{\phi}_C$ and (iii) domain (batch) discriminator, $D_{\boldsymbol{\phi}_D}(E_{\boldsymbol{\phi}}(\boldsymbol{x}_n))$. The model has a Siamese design and the training takes a pair of cells $(\boldsymbol{x}_1, \boldsymbol{x}_2)$, each from the same or different batches. The encoder network contains two hidden layers with 1146 and 100 neurons. $C_{\boldsymbol{\phi}_C}$ classifies the cell type and $D_{\boldsymbol{\phi}_D}$ predicts whether $\boldsymbol{x}_1$ and $\boldsymbol{x}_2$ are from the same batch or not. The overall loss is denoted by

$$L(\boldsymbol{\phi}, \boldsymbol{\phi}_C, \boldsymbol{\phi}_D) = L_C\left(C_{\boldsymbol{\phi}_C}\left(E_{\boldsymbol{\phi}}(\boldsymbol{x}_1)\right)\right) - \lambda L_D\left(D_{\boldsymbol{\phi}_D}\left(E_{\boldsymbol{\phi}}(\boldsymbol{x}_1)\right), D_{\boldsymbol{\phi}_D}\left(E_{\boldsymbol{\phi}}(\boldsymbol{x}_2)\right)\right), \quad (37)$$

where L_C is the cross-entropy loss, and L_D is a contrastive loss as described in [104]. Notice that Eq. (37) has an adversarial formulation and minimizing this loss maximizes the misclassification of cells from different batches, thus making them indistinguishable. Similar to GAN training, scDGN is trained to iteratively solve: $\hat{\boldsymbol{\phi}}_D = \mathbf{argmin}_{\boldsymbol{\phi}_D} L(\hat{\boldsymbol{\phi}}, \hat{\boldsymbol{\phi}}_C, \boldsymbol{\phi}_D)$ and $(\hat{\boldsymbol{\phi}}, \hat{\boldsymbol{\phi}}_C) = \mathbf{argmin}_{\boldsymbol{\phi}, \boldsymbol{\phi}_C} L(\boldsymbol{\phi}, \boldsymbol{\phi}_C, \hat{\boldsymbol{\phi}}_D)$.

Results

scDGN was tested for classifying cell types and aligning batches ranging in size from 10 to 39 cell types and from 4 to 155 batches. The performance was compared with a series of DL and traditional ML methods, including Lin *et al.* DNN [71], CaSTLe [105], MNN [32], scVI [17] and Seurat [10]. scDGN outperformed all other methods in the classification accuracy on a subset of scQuery datasets (0.29), PBMC (0.87) and four of the six Seurat pancreatic datasets (0.86–0.95). PCA visualization of the learned data representations demonstrated that scDGN overcame the batch differences and clearly separated cell clusters based on cell types, while other methods were vulnerable to batch effects. In summary, scDGN is a supervised adversarial alignment method to eliminate the batch effect of scRNA-seq data and create cleaner representations of cell types.

Biological function prediction

Predicting biological functions and responses to treatment at single cell level or cell types is critical to understand cellular system functioning and potent responses to stimulations. DL models are capable of capture gene–gene relationship and their property in the latent space. Several surveyed models demonstrate exciting results to learn complex biological functions and outcomes.

CNN for coexpression

CNNC [54] is proposed to infer causal interactions between genes from scRNA-seq data.

Model

CNNC is a CNN (Figure 4F), one of the most popular DL models. CNNC takes expression levels of two genes from many cells and transforms them into a 32×32 image-like normalized empirical probability function (NEPDF), which measures the probabilities of observing different coexpression levels between the two genes. CNNC includes six convolutional layers, three max-pooling layers, one flatten layer and one output layer. All convolution layers have 32 kernels of size 3×3. Depending on the application, the output layer can be designed to predict the state of interaction (Yes/No) between the genes or the causal interaction between the input genes (no interaction, gene A regulates gene B or gene B regulates gene A).

Result

CNNC was trained to predict TF-Gene interactions using the mESC data from scQuery [106], where the ground truth interactions were obtained from the ChIP-seq dataset from the GTRD database [107]. The performance was compared with DNN, count statistics [108] and mutual information (MI)-based approach [109]. CNNC was shown to have more than 20% higher AUPRC than other methods and reported almost no false-negative for the top 5% predictions. CNNC was also trained to predict the pathway regulator-target gene pairs. The positive regulator-gene pairs were obtained from KEGG [110] and Reactome [111], and negative samples were genes pairs that appeared in pathways but do not interacted. CNNC was shown to have better performance of predicting regulator-gene pairs on both KEGG and Reactome pathways than other methods including Pearson correlation, count statistics, GENIE3 [112], MI, Bayesian-directed network (BDN) and DREMI

[109]. CNNC was also applied for causality prediction between two genes, that is if two genes regulate each other and if they do, which gene is the regulator. The ground truth causal relationships were also obtained from the KEGG and Reactome datasets. Again, CNNC reported better performance than BDN, the common method developed to learn casual relationships from gene expression data. CNNC was finally trained to assign three essential cell functions (cell cycle, circadian rhythm and immune system) to genes. This is achieved by training CNNC to predict pairs of genes from the same function (e.g. Cell Cycle defined by mSigDB from gene set enrichment analysis [113]) as 1 and all other pairs as 0. The performance was compared with 'guilt by association' and DNN, and CNNC was shown to have more than 4% higher AUROC and reported all positives for the top 10% predictions.

scGen, a generative model to predict perturbation response of single cells across cell types

scGen [114] is designed to learn cellular responses to certain perturbations such as drug treatment and gene knockout from single-cell expression data, and then predict cellular responses to the same perturbation for a new sample or a new cell type. The novelty of scGen is that it learns the cellular response in the latent space instead of the expression data space.

Model

ScGen follows the general VAE (Figures 2A and 4C) for scRNA-seq data but uses the 'latent space arithmetics' to learn perturbations' response. Given scRNA-seq samples of perturbed (denoted as *p*) and unperturbed cells (denoted as *unp*), a VAE model is trained. Then, the latent space representation $\mathbf{z}_p$ and $\mathbf{z}_{unp}$ are obtained for the perturbed and unperturbed cells. Following the notion that VAE could map nonlinear operations (e.g. perturbation) in the data space to linear operations in the latent space, ScGen estimates the response in the latent space as $\boldsymbol{\delta} = \overline{\mathbf{z}}_p - \overline{\mathbf{z}}_{unp}$, where $\overline{\mathbf{z}}_.$ is the average representation of samples from the same cell type or different cell types. Then, given the latent representation $\mathbf{z}'_{unp}$ of an unperturbed cell for a new sample from the same or different cell type, the latent representation of the corresponding perturbed cell can be predicted as $\mathbf{z}'_p = \mathbf{z}'_{unp} + \boldsymbol{\delta}$. The expression of the perturbed cell can also be estimated by feeding $\mathbf{z}'_p$ into the VAE decoder. The scGen can also be expanded to samples and treatment across two species (using orthologues between species). When scGen is trained for species 1 (s_1) with both perturbed and unperturbed cells and species 2 (s_2) with only unperturbed cells, the latent code for the perturbed cells from s_2 can be predicted as $\mathbf{z}_{s_2,p} = \frac{1}{2}(z_{s_1,p} + z_{s_2,unp} + \delta_s + \delta_p)$ where $\boldsymbol{\delta}_p = z_{s_1,unp} - z_{s_1,p}$ captures the response of perturbation and $\boldsymbol{\delta}_s = z_{s_1} - z_{s_2}$ represents the difference between species.

Result

scGen was applied to predict the perturbation of out-of-samples response in human PBMCs data, and scGen showed a higher average correlation ($R^2 = 0.948$) between predicted and real data for six cell types [115]. Compared with other methods including CVAE [116], style transfer GAN [117], linear approaches based on vector arithmetics (VA) similar in [118] and PCA + VA, scGen predicted full distribution of ISG15 gene (strongest regulated gene by IFN-β) response to IFN-β [115], while others might predict mean (CAVE and style transfer GAN) but failed to produce the full distribution. scGen was also tested on predicting the intestinal epithelial cells' response to infections [119]. For early transit-amplifying cells, scGen showed good prediction ($R^2 = 0.98$) for both *Heligmosomoides polygyrus* and *Salmonella* infections. Finally, scGen was evaluated for perturbation across species using scRNA-seq data set by Hagai *et al.* [120], which comprises bone marrow-derived mononuclear phagocytes from mice, rats, rabbits and pigs perturbed with lipopolysaccharide (LPS). scGen's predictions of LPS perturbation responses were shown to be highly correlated ($R^2 = 0.91$) with the real responses.

CONCLUSIONS

We systematically survey 25 DL models according to the challenges they address. We categorize major DL model statements into VAE, AE and GAN with a unified mathematic formulation in Section 3 (graphic model representation in Figure 2), which will guide readers to focus on the DL model selection, training strategies and loss functions in each algorithm. Specifically, the differences in loss functions are highlighted in each DL model's applications to meet specific objectives. DL/ML models that 25 surveyed models are evaluated against are presented in Figure 3, providing a straightforward way for readers to pick up the most suitable DL model at a specific step for their own scRNA-seq data analysis. All evaluation methods are listed in Table 8, as we foresee Table 8 to be an easy recipe book for researchers to establish their scRNA-seq pipeline. In addition, a summary of all the 25 DL models concerning their DL models, evaluation metrics, implementation environment, downloadable source codes, features and application notes is presented in **Tables 1** and **2**. Taken together, this survey provides a rich resource to select a DL model for proper research applications, and we expect to inspire new DL model developments for scRNA-seq analysis.

One advantage of DL for scRNA-seq repeatedly demonstrated in many of these surveyed papers is DL's ability to scale to a large number of cells, thanks to the stochastic gradient descent algorithm. For imputation, DCA shows linear scalability with the number of cells, and scIGAN and DeepInpute are demonstrated to scale to 100-K cells, while non-DL algorithms including SAVER and SCRABBLE fail due to excessive memory usage and runtime [19]. A similar favorable scalability result has been echoed for batch normalization by DESC and iMAP, clustering by scDeepCluster, and multi-functional analysis by scVI, LDVAE, SAUCIE and scScope. Overall, the advantage of DL in scalability becomes more apparent over non-DL approaches after the number of cells exceeds thousands. However, many of these comparisons exclude the time for determining DL models' hyperparameters. Although iMAP shows that the model is robust against model hyperparameters, determinination of optimal hyperparameters in DL models has not been comprehensively studied for these scRNA-seq tasks.

This review focuses on surveying common DL models, such as AE, VAE and GAN, and their model variations or combinations to address single-cell data analysis challenges. With the advancement of multi-omics single-cell technologies, new single-cell data types and DL models will be introduced to the single-cell analysis pipeline, such as cyTOF using SAUCIE [15], spatial transcriptome using DNN [121] and CITE-seq that simultaneously generates read counts for surface protein expression along with gene expression [122, 123]. Other than three most common unsupervised DL models using AE, VAE and GAN, this review also discusses supervised network frameworks including CapsNet (e.g. scCapsNet [52]), CNN (e.g. CNNC [54]) and domain adaption learning (e.g. scDGN [53]). It is expected that more DL models and learning paradigms will be developed and implemented for the most challenging steps for scRNA-seq data, including but not limited to, multi-omics data integration and data interpretation. For example, integrating PPI graphs into DL models has been shown for its advantages of biological knowledge and nonlinear interactions embedded in the graphs [124–126]. Indeed, a recently published scRNA-seq analysis pipeline, scGNN [127], incorporates three iterative AEs (including one graph AE) and successfully demonstrated Alzheimer's disease-related neural development and differentiation mechanisms. We expect that our careful organization of this review will provide a basic understanding of DL models for scRNA-seq and inspire innovative applications of DL models for single cell analysis.

Authors' contributions

Y.H., Y.C., M.F. and Y.F.J. conceived the study. M.F., Z.L., T.Z., M.M.H., Y.C.C., Z.Y., K.P., S.J., J.Z., S.J.G., Y.F.J., Y.C. and Y.H. summarized resources, wrote and approved the final version of the paper.

Key Points

- Single cell RNA sequencing technology generates a large collection of transcriptomic profiles of up to millions of cells, enabling biological investigation of hidden expression functional structures or cell types, predicting their effects or responses to treatment more precisely or utilizing subpopulations to address unanswered hypotheses.
- Twenty-five deep learning-based approaches for single cell RNA seq data analysis are systematically reviewed in this paper according to the challenge they address and their roles in the analysis pipeline.
- A unified mathematical description of the surveyed DL models is presented and the specific model features were discussed when reviewing each approach.
- A comprehensive summary of the evaluation metrics, comparison algorithms and datasets by each approach is presented.

Funding

National Institutes of Health (grant no. CTSA 1UL1RR025 767-01 to Y.C., R01GM113245 to Y.H., NCI Cancer Center Shared Resources P30CA54174 to Y.C., K99CA248944 to Y.C.C.); National Science Foundation (grant no. 2051113 to Y.F.J.); Cancer Prevention and Research Institute of Texas (grant no. RP160732 to Y.C., RP190346 to Y.C. and Y.H.); Fund for Innovation in Cancer Informatics (ICI Fund to Y.C.C. and Y.C.). The funding sources had no role in the design of the study; collection, analysis and interpretation of data; or in writing the manuscript.

References

1. Lahnemann D, Koster J, Szczurek E, *et al.* Eleven grand challenges in single-cell data science. *Genome Biol* 2020;**21**(1):31.
2. Vitak SA, Torkenczy KA, Rosenkrantz JL, *et al.* Sequencing thousands of single-cell genomes with combinatorial indexing. *Nat Methods* 2017;**14**(3):302–8.
3. Wu H, Wang C, Wu S. Single-cell sequencing for drug discovery and drug development. *Curr Top Med Chem* 2017;**17**(15):1769–77.
4. Kinker GS, Greenwald AC, Tal R, *et al.* Pan-cancer single-cell RNA-seq identifies recurring programs of cellular heterogeneity. *Nat Genet* 2020;**52**(11):1208–18.
5. Navin NE. The first five years of single-cell cancer genomics and beyond. *Genome Res* 2015;**25**(10):1499–507.
6. Suva ML, Tirosh I. Single-cell RNA sequencing in cancer: lessons learned and emerging challenges. *Mol Cell* 2019;**75**(1): 7–12.
7. Mannarapu M, Dariya B, Bandapalli OR. Application of single-cell sequencing technologies in pancreatic cancer. *Mol Cell Biochem* 2021;**476**(6):2429–37.
8. Wauters E, Van Mol P, Garg AD, *et al.* Discriminating mild from critical COVID-19 by innate and adaptive immune single-cell profiling of bronchoalveolar lavages. *Cell Res* 2021;**31**(3):272–90.
9. Bost P, Giladi A, Liu Y, *et al.* Host-viral infection maps reveal signatures of severe COVID-19 patients. *Cell* 2020;**181**(7):1475–1488.e12.
10. Stuart T, Butler A, Hoffman P, *et al.* Comprehensive integration of single-cell data. *Cell* 2019;**177**(7):1888–1902.e21.
11. Wolf FA, Angerer P, Theis FJ. SCANPY: large-scale single-cell gene expression data analysis. *Genome Biol* 2018;**19**(1):15.
12. Vaswani A, Shazeer N, Parmar N, *et al.* Attention is all you need. In: *Advances in neural information processing systems*, 2017, 5998–6008.
13. Karpathy A, Toderici G, Shetty S, Leung T, Sukthankar R, Fei-Fei L: Large-scale video classification with convolutional neural networks. In: *Proceedings of the IEEE conference on Computer Vision and Pattern Recognition*, 2014. 1725–32.
14. Deng L, Liu Y. *Deep learning in natural language processing*. Springer, 2018.

15. Amodio M, van Dijk D, Srinivasan K, *et al.* Exploring single-cell data with deep multitasking neural networks. *Nat Methods* 2019;**16**(11):1139–45.
16. Srinivasan S, Leshchyk A, Johnson NT, *et al.* A hybrid deep clustering approach for robust cell type profiling using single-cell RNA-seq data. *RNA* 2020;**26**(10):1303–19.
17. Lopez R, Regier J, Cole MB, *et al.* Deep generative modeling for single-cell transcriptomics. *Nat Methods* 2018;**15**(12):1053–8.
18. Eraslan G, Simon LM, Mircea M, *et al.* Single-cell RNA-seq denoising using a deep count autoencoder. *Nat Commun* 2019;**10**(1):390.
19. Xu Y, Zhang Z, You L, *et al.* scIGANs: single-cell RNA-seq imputation using generative adversarial networks. *Nucleic Acids Res* 2020;**48**(15):e85.
20. Arisdakessian C, Poirion O, Yunits B, *et al.* DeepImpute: an accurate, fast, and scalable deep neural network method to impute single-cell RNA-seq data. *Genome Biol* 2019;**20**(1):211.
21. Tran HTN, Ang KS, Chevrier M, *et al.* A benchmark of batch-effect correction methods for single-cell RNA sequencing data. *Genome Biol* 2020;**21**(1):12.
22. Petegrosso R, Li Z, Kuang R. Machine learning and statistical methods for clustering single-cell RNA-sequencing data. *Brief Bioinform* 2020;**21**(4):1209–23.
23. Abdelaal T, Michielsen L, Cats D, *et al.* A comparison of automatic cell identification methods for single-cell RNA sequencing data. *Genome Biol* 2019;**20**(1):194.
24. Wang J, Zou Q, Lin C. A comparison of deep learning-based pre-processing and clustering approaches for single-cell RNA sequencing data. *Brief Bioinform* 2021. https://doi.org/10.1093/bib/bbab345.
25. Picelli S, Bjorklund AK, Faridani OR, *et al.* Smart-seq2 for sensitive full-length transcriptome profiling in single cells. *Nat Methods* 2013;**10**(11):1096–8.
26. Macosko EZ, Basu A, Satija R, *et al.* Highly parallel genome-wide expression profiling of individual cells using Nanoliter droplets. *Cell* 2015;**161**(5):1202–14.
27. Eisenstein M. Single-cell RNA-seq analysis software providers scramble to offer solutions. *Nat Biotechnol* 2020;**38**(3):254–7.
28. Chen G, Ning B, Shi T. Single-cell RNA-Seq technologies and related computational data analysis. *Front Genet* 2019;**10**:317.
29. Vallejos CA, Marioni JC, Richardson S. BASiCS: Bayesian analysis of single-cell sequencing data. *PLoS Comput Biol* 2015;**11**(6):e1004333.
30. Lun AT, Bach K, Marioni JC. Pooling across cells to normalize single-cell RNA sequencing data with many zero counts. *Genome Biol* 2016;**17**:75.
31. Hafemeister C, Satija R. Normalization and variance stabilization of single-cell RNA-seq data using regularized negative binomial regression. *Genome Biol* 2019;**20**(1):296.
32. Haghverdi L, Lun ATL, Morgan MD, *et al.* Batch effects in single-cell RNA-sequencing data are corrected by matching mutual nearest neighbors. *Nat Biotechnol* 2018;**36**(5):421–7.
33. Butler A, Hoffman P, Smibert P, *et al.* Integrating single-cell transcriptomic data across different conditions, technologies, and species. *Nat Biotechnol* 2018;**36**(5):411–20.
34. Korsunsky I, Millard N, Fan J, *et al.* Fast, sensitive and accurate integration of single-cell data with harmony. *Nat Methods* 2019;**16**(12):1289–96.
35. Peng T, Zhu Q, Yin P, *et al.* SCRABBLE: single-cell RNA-seq imputation constrained by bulk RNA-seq data. *Genome Biol* 2019;**20**(1):88.
36. Huang M, Wang J, Torre E, *et al.* SAVER: gene expression recovery for single-cell RNA sequencing. *Nat Methods* 2018;**15**(7):539–42.
37. Li WV, Li JJ. An accurate and robust imputation method scImpute for single-cell RNA-seq data. *Nat Commun* 2018;**9**(1):997.
38. Roweis ST, Saul LK. Nonlinear dimensionality reduction by locally linear embedding. *Science* 2000;**290**(5500):2323–6.
39. Welch JD, Hartemink AJ, Prins JF. SLICER: inferring branched, nonlinear cellular trajectories from single cell RNA-seq data. *Genome Biol* 2016;**17**(1):106.
40. Linderman GC, Rachh M, Hoskins JG, *et al.* Fast interpolation-based t-SNE for improved visualization of single-cell RNA-seq data. *Nat Methods* 2019;**16**(3):243–5.
41. Becht E, McInnes L, Healy J, *et al.* Dimensionality reduction for visualizing single-cell data using UMAP. *Nat Biotechnol* 2019;**37**(1):38–44.
42. Subelj L, Bajec M. Unfolding communities in large complex networks: combining defensive and offensive label propagation for core extraction. *Phys Rev E Stat Nonlin Soft Matter Phys* 2011;**83**(3):036103.
43. Traag VA, Waltman L, van Eck NJ. From Louvain to Leiden: guaranteeing well-connected communities. *Sci Rep* 2019;**9**(1):5233.
44. Wang B, Zhu J, Pierson E, *et al.* Visualization and analysis of single-cell RNA-seq data by kernel-based similarity learning. *Nat Methods* 2017;**14**(4):414–6.
45. Finak G, McDavid A, Yajima M, *et al.* MAST: a flexible statistical framework for assessing transcriptional changes and characterizing heterogeneity in single-cell RNA sequencing data. *Genome Biol* 2015;**16**:278.
46. Kharchenko PV, Silberstein L, Scadden DT. Bayesian approach to single-cell differential expression analysis. *Nat Methods* 2014;**11**(7):740–2.
47. Miao Z, Deng K, Wang X, *et al.* DEsingle for detecting three types of differential expression in single-cell RNA-seq data. *Bioinformatics* 2018;**34**(18):3223–4.
48. Goodfellow I, Pouget-Abadie J, Mirza M, *et al.* Generative adversarial networks. *Commun ACM* 2020;**63**(11):139–44.
49. Gulrajani I, Ahmed F, Arjovsky M, *et al.* Improved training of wasserstein gans. *arXiv preprint arXiv:170400028*. 2017.
50. Arjovsky M, Chintala S, Bottou L. Wasserstein Gan. *arXiv* 2017*arXiv preprint arXiv:170107875*;**2017**:30.
51. Torroja C, Sanchez-Cabo F. Digitaldlsorter: deep-learning on scRNA-Seq to deconvolute gene expression data. *Front Genet* 2019;**10**:978.
52. Wang L, Nie R, Yu Z, *et al.* An interpretable deep-learning architecture of capsule networks for identifying cell-type gene expression programs from single-cell RNA-sequencing data. *Nat Mach Intell* 2020;**2**:693–703.
53. Ge S, Wang H, Alavi A, *et al.* Supervised adversarial alignment of single-cell RNA-seq data. *J Comput Biol* 2021;**28**(5):501–13.
54. Yuan Y, Bar-Joseph Z. Deep learning for inferring gene relationships from single-cell expression data. *Proc Natl Acad Sci U S A* 2019;**116**(52):27151–8.
55. Eraslan G, Avsec Z, Gagneur J, *et al.* Deep learning: new computational modelling techniques for genomics. *Nat Rev Genet* 2019;**20**(7):389–403.
56. Patel ND, Nguang SK, Coghill GG. Neural network implementation using bit streams. *IEEE Trans Neural Netw* 2007;**18**(5):1488–504.
57. van Dijk D, Sharma R, Nainys J, *et al.* Recovering gene interactions from single-cell data using data diffusion. *Cell* 2018;**174**(3):716–729.e27.
58. Wang J, Agarwal D, Huang M, *et al.* Data denoising with transfer learning in single-cell transcriptomics. *Nat Methods* 2019;**16**(9):875–8.

59. Badsha MB, Li R, Liu B, *et al.* Imputation of single-cell gene expression with an autoencoder neural network. *Quant Biol* 2020;**8**(1):78–94.
60. Yu B, Chen C, Qi R, *et al.* scGMAI: a Gaussian mixture model for clustering single-cell RNA-Seq data based on deep autoencoder. *Brief Bioinform* 2021;**22**(4).
61. Lin P, Troup M, Ho JW. CIDR: ultrafast and accurate clustering through imputation for single-cell RNA-seq data. *Genome Biol* 2017;**18**(1):59.
62. Berthelot D, Schumm T, Metz L. BEGAN: boundary equilibrium generative adversarial networks. *arXiv* 2017.
63. Wang T, Johnson TS, Shao W, *et al.* BERMUDA: a novel deep transfer learning method for single-cell RNA sequencing batch correction reveals hidden high-resolution cellular subtypes. *Genome Biol* 2019;**20**(1):165.
64. Borgwardt KM, Gretton A, Rasch MJ, *et al.* Integrating structured biological data by kernel maximum mean discrepancy. *Bioinformatics* 2006;**22**(14):e49–57.
65. Crow M, Paul A, Ballouz S, *et al.* Characterizing the replicability of cell types defined by single cell RNA-sequencing data using MetaNeighbor. *Nat Commun* 2018;**9**(1):884.
66. Polanski K, Young MD, Miao Z, *et al.* BBKNN: fast batch alignment of single cell transcriptomes. *Bioinformatics* 2020;**36**(3): 964–5.
67. Li X, Wang K, Lyu Y, *et al.* Deep learning enables accurate clustering with batch effect removal in single-cell RNA-seq analysis. *Nat Commun* 2020;**11**(1):2338.
68. Guo X, Gao L, Liu X, Yin J. Improved deep embedded clustering with local structure preservation. In: *Proc 26th International Joint Conference on Artificial Integlligence*, 2017:1753–9.
69. Hie B, Bryson B, Berger B. Efficient integration of heterogeneous single-cell transcriptomes using Scanorama. *Nat Biotechnol* 2019;**37**(6):685–91.
70. Wang D, Hou S, Zhang L, *et al.* iMAP: integration of multiple single-cell datasets by adversarial paired transfer networks. *Genome Biol* 2021;**22**(1):63.
71. Lin C, Jain S, Kim H, *et al.* Using neural networks for reducing the dimensions of single-cell RNA-Seq data. *Nucleic Acids Res* 2017;**45**(17):e156.
72. Rashid S, Shah S, Bar-Joseph Z, *et al.* Dhaka: Variational autoencoder for unmasking tumor heterogeneity from single cell genomic data. *Bioinformatics* 2021;**37**(11):1535–43.
73. Tirosh I, Izar B, Prakadan SM, *et al.* Dissecting the multicellular ecosystem of metastatic melanoma by single-cell RNA-seq. *Science* 2016;**352**(6282):189–96.
74. Zahn H, Steif A, Laks E, *et al.* Scalable whole-genome single-cell library preparation without preamplification. *Nat Methods* 2017;**14**(2):167–73.
75. Ding J, Condon A, Shah SP. Interpretable dimensionality reduction of single cell transcriptome data with deep generative models. *Nat Commun* 2018;**9**(1):2002.
76. Gronbech CH, Vording MF, Timshel PN, *et al.* scVAE: variational auto-encoders for single-cell gene expression data. *Bioinformatics* 2020;**36**(16):4415–22.
77. Wang D, Gu J. VASC: dimension reduction and visualization of single-cell RNA-seq data by deep variational autoencoder. *Genomics Proteomics Bioinformatics* 2018;**16**(5):320–31.
78. Jang E. GSaPB: categorical reparameterization with gumbel-softmax. *arXiv* 2016.
79. Tian T, Wan J, Song Q, *et al.* Clustering single-cell RNA-seq data with a model-based deep learning approach. *Nat Mach Intell* 2019;**1**(4):191–8.
80. Regev A, Teichmann SA, Lander ES, *et al.* The human cell atlas. *Elife* 2017;**6**.
81. Xie J, Girshick R, Farhadi A: Unsupervised deep embedding for clustering analysis. In: *International conference on machine learning*, 2016. 478–87. PMLR.
82. Marouf M, Machart P, Bansal V, *et al.* Realistic in silico generation and augmentation of single-cell RNA-seq data using generative adversarial networks. *Nat Commun* 2020;**11**(1):166.
83. Miyato TaK M. cGANs with projection discriminator. In press. 2018.
84. Zappia L, Phipson B, Oshlack A. Splatter: simulation of single-cell RNA sequencing data. *Genome Biol* 2017;**18**(1):174.
85. Lindenbaum O, Stanley JS, Wolf G, *et al.* Geometry-based data generation. In: *Advances in Neural Information Processing Systems*, 2018.
86. Svensson V, Gayoso A, Yosef N, *et al.* Interpretable factor models of single-cell RNA-seq via variational autoencoders. *Bioinformatics* 2020;**36**(11):3418–21.
87. Levine JH, Simonds EF, Bendall SC, *et al.* Data-driven phenotypic dissection of AML reveals progenitor-like cells that correlate with prognosis. *Cell* 2015;**162**(1):184–97.
88. Qiu X, Mao Q, Tang Y, *et al.* Reversed graph embedding resolves complex single-cell trajectories. *Nat Methods* 2017;**14**(10): 979–82.
89. McInnes L, Healy J, Melville J. Umap: uniform manifold approximation and projection for dimension reduction. *ArXiv* 2018.
90. van der Maaten L, Hinton G. Visualizing data using t-SNE. *J Mach Learn* 2008;**9**:2579–605.
91. Moon KR, Dijk DV, Wang Z, *et al.* PHATE: a dimensionality reduction method for visualizing trajectory structures in high-dimensional biological data. *bioRxiv* 2017.
92. Deng Y, Bao F, Dai Q, *et al.* Scalable analysis of cell-type composition from single-cell transcriptomics using deep recurrent learning. *Nat Methods* 2019;**16**(4):311–4.
93. Chung W, Eum HH, Lee HO, *et al.* Single-cell RNA-seq enables comprehensive tumour and immune cell profiling in primary breast cancer. *Nat Commun* 2017;**8**:15081.
94. Li H, Courtois ET, Sengupta D, *et al.* Reference component analysis of single-cell transcriptomes elucidates cellular heterogeneity in human colorectal tumors. *Nat Genet* 2017;**49**(5): 708–18.
95. Aran D, Hu Z, Butte AJ. xCell: digitally portraying the tissue cellular heterogeneity landscape. *Genome Biol* 2017;**18**(1):220.
96. Yoshihara K, Shahmoradgoli M, Martinez E, *et al.* Inferring tumour purity and stromal and immune cell admixture from expression data. *Nat Commun* 2013;**4**:2612.
97. Racle J, de Jonge K, Baumgaertner P, *et al.* Simultaneous enumeration of cancer and immune cell types from bulk tumor gene expression data. *Elife* 2017;**6**.
98. Becht E, Giraldo NA, Lacroix L, *et al.* Estimating the population abundance of tissue-infiltrating immune and stromal cell populations using gene expression. *Genome Biol* 2016;**17**(1): 218.
99. Zheng GX, Terry JM, Belgrader P, *et al.* Massively parallel digital transcriptional profiling of single cells. *Nat Commun* 2017;**8**:14049.
100. Shekhar K, Lapan SW, Whitney IE, *et al.* Comprehensive classification of retinal bipolar neurons by single-cell transcriptomics. *Cell* 2016;**166**(5):1308–1323.e30.
101. Dong Z, Alterovitz G. netAE: semi-supervised dimensionality reduction of single-cell RNA sequencing to facilitate cell labeling. *Bioinformatics* 2021;**37**(1):43–9.

102. Newman ME. Modularity and community structure in networks. *Proc Natl Acad Sci U S A* 2006;**103**(23):8577–82.
103. Xu C, Lopez R, Mehlman E, *et al.* Probabilistic harmonization and annotation of single-cell transcriptomics data with deep generative models. *Mol Syst Biol* 2021;**17**(1):e9620.
104. Hadsell R, Chopra S, Le Cun Y: Dimensionality reduction by learning an invariant mapping. In: *2006 IEEE Computer Society Conference on Computer Vision and Pattern Recognition (CVPR'06)*, 2006. 1735–42. IEEE.
105. Lieberman Y, Rokach L, Shay T. CaSTLe–classification of single cells by transfer learning: harnessing the power of publicly available single cell RNA sequencing experiments to annotate new experiments. *PLoS One* 2018;**13**(10):e0205499.
106. Alavi A, Ruffalo M, Parvangada A, *et al.* A web server for comparative analysis of single-cell RNA-seq data. *Nat Commun* 2018;**9**(1):4768.
107. Yevshin I, Sharipov R, Valeev T, *et al.* GTRD: a database of transcription factor binding sites identified by ChIP-seq experiments. *Nucleic Acids Res* 2016;**45**(D1):D61–7.
108. Wang YXR, Waterman MS, Huang HY. Gene coexpression measures in large heterogeneous samples using count statistics. *P Natl Acad Sci USA* 2014;**111**(46):16371–6.
109. Krishnaswamy S, Spitzer MH, Mingueneau M, *et al.* Systems biology. Conditional density-based analysis of T cell signaling in single-cell data. *Science* 2014;**346**(6213):1250689.
110. Kanehisa M, Furumichi M, Tanabe M, *et al.* KEGG: new perspectives on genomes, pathways, diseases and drugs. *Nucleic Acids Res* 2017;**45**(D1):D353–61.
111. Fabregat A, Jupe S, Matthews L, *et al.* The Reactome pathway knowledgebase. *Nucleic Acids Res* 2018;**46**(D1):D649–55.
112. Huynh-Thu VA, Irrthum A, Wehenkel L, *et al.* Inferring regulatory networks from expression data using tree-based methods. *PLoS One* 2010;**5**(9):e12776.
113. Subramanian A, Tamayo P, Mootha VK, *et al.* Gene set enrichment analysis: a knowledge-based approach for interpreting genome-wide expression profiles. *Proc Natl Acad Sci U S A* 2005;**102**(43):15545–50.
114. Lotfollahi M, Wolf FA, Theis FJ. scGen predicts single-cell perturbation responses. *Nat Methods* 2019;**16**(8):715–21.
115. Kang HM, Subramaniam M, Targ S, *et al.* Multiplexed droplet single-cell RNA-sequencing using natural genetic variation. *Nat Biotechnol* 2018;**36**(1):89–94.
116. Duvenaud D, Maclaurin D, Iparraguirre J, *et al.* In: Cortes C, Lawrence ND, Lee DD *et al.* (eds). *Advances in Neural Information Processing Systems* 28, 2015, 2224–32.
117. Amodio M, Krishnaswamy S: MAGAN: Aligning biological manifolds. In: *International Conference on Machine Learning*, 2018. 215–23. PMLR.
118. Ghahramani A, Watt FM, Luscombe NM. Generative adversarial networks simulate gene expression and predict perturbations in single cells. *bioRxiv* 2018;262501.
119. Haber AL, Biton M, Rogel N, *et al.* A single-cell survey of the small intestinal epithelium. *Nature* 2017;**551**(7680):333–9.
120. Hagai T, Chen X, Miragaia RJ, *et al.* Gene expression variability across cells and species shapes innate immunity. *Nature* 2018;**563**(7730):197–202.
121. Maseda F, Cang Z, Nie Q. DEEPsc: a deep learning-based map connecting single-cell transcriptomics and spatial imaging data. *Front Genet* 2021;**12**:636743.
122. Musu Y, Liang C, Deng M. Clustering single cell CITE-seq data with a canonical correlation based deep learning method. *bioRxiv* 2021.
123. Zhou Z, Ye C, Wang J, *et al.* Surface protein imputation from single cell transcriptomes by deep neural networks. *Nat Commun* 2020;**11**(1):651.
124. Ramirez R, Chiu Y-C, Hererra A, *et al.* Classification of cancer types using graph convolutional neural networks. *Frontiers in Physics* 2020;**8**(203). https://doi.org/10.3389/fphy.2020.00203.
125. Ramirez R, Chiu YC, Zhang S, *et al.* Prediction and interpretation of cancer survival using graph convolution neural networks. *Methods* 2021;**192**:120–30.
126. Battaglia PW, Hamrick JB, Bapst V, *et al.* Relational inductive biases, deep learning, and graph networks *arXiv preprint arXiv:180601261*. 2018.
127. Wang J, Ma A, Chang Y, *et al.* scGNN is a novel graph neural network framework for single-cell RNA-Seq analyses. *Nat Commun* 2021;**12**(1):1882.
128. Peng Y, Baulier E, Ke Y, *et al.* Human embryonic stem cells extracellular vesicles and their effects on immortalized human retinal Muller cells. *PLoS One* 2018;**13**(3):e0194004.
129. Stoeckius M, Hafemeister C, Stephenson W, *et al.* Simultaneous epitope and transcriptome measurement in single cells. *Nat Methods* 2017;**14**(9):865–8.
130. La Manno G, Gyllborg D, Codeluppi S, *et al.* Molecular diversity of midbrain development in mouse, human, and stem cells. *Cell* 2016;**167**(2):566–580 e519.
131. Azizi E, Carr AJ, Plitas G, *et al.* Single-cell map of diverse immune phenotypes in the breast tumor microenvironment. *Cell* 2018;**174**(5):1293–1308.e36.
132. Chu LF, Leng N, Zhang J, *et al.* Single-cell RNA-seq reveals novel regulators of human embryonic stem cell differentiation to definitive endoderm. *Genome Biol* 2016;**17**(1):173.
133. Baron M, Veres A, Wolock SL, *et al.* A single-cell transcriptomic map of the human and mouse pancreas reveals inter- and intra-cell population structure. *Cell Syst* 2016;**3**(4):346–360.e4.
134. Camp JG, Sekine K, Gerber T, *et al.* Multilineage communication regulates human liver bud development from pluripotency. *Nature* 2017;**546**(7659):533–8.
135. Muraro MJ, Dharmadhikari G, Grun D, *et al.* A single-cell transcriptome atlas of the human pancreas. *Cell Syst* 2016;**3**(4):385–394.e3.
136. Darmanis S, Sloan SA, Zhang Y, *et al.* A survey of human brain transcriptome diversity at the single cell level. *Proc Natl Acad Sci U S A* 2015;**112**(23):7285–90.
137. Tirosh I, Venteicher AS, Hebert C, *et al.* Single-cell RNA-seq supports a developmental hierarchy in human oligodendroglioma. *Nature* 2016;**539**(7628):309–13.
138. Patel AP, Tirosh I, Trombetta JJ, *et al.* Single-cell RNA-seq highlights intratumoral heterogeneity in primary glioblastoma. *Science* 2014;**344**(6190):1396–401.
139. Pollen AA, Nowakowski TJ, Shuga J, *et al.* Low-coverage single-cell mRNA sequencing reveals cellular heterogeneity and activated signaling pathways in developing cerebral cortex. *Nat Biotechnol* 2014;**32**(10):1053–8.
140. Xin Y, Kim J, Okamoto H, *et al.* RNA sequencing of single human islet cells reveals type 2 diabetes genes. *Cell Metab* 2016;**24**(4):608–15.
141. Yan L, Yang M, Guo H, *et al.* Single-cell RNA-Seq profiling of human preimplantation embryos and embryonic stem cells. *Nat Struct Mol Biol* 2013;**20**(9):1131–9.
142. Chevrier S, Levine JH, Zanotelli VRT, *et al.* An immune atlas of clear cell renal cell carcinoma. *Cell* 2017;**169**(4):736–749.e18.
143. Han X, Wang R, Zhou Y, *et al.* Mapping the mouse cell atlas by microwell-Seq. *Cell* 2018;**172**(5):1091–1107.e17.

144. Hrvatin S, Hochbaum DR, Nagy MA, *et al.* Single-cell analysis of experience-dependent transcriptomic states in the mouse visual cortex. *Nat Neurosci* 2018;**21**(1): 120–9.
145. Joost S, Zeisel A, Jacob T, *et al.* Single-cell transcriptomics reveals that differentiation and spatial signatures shape epidermal and hair follicle heterogeneity. *Cell Syst* 2016;**3**(3): 221–237.e9.
146. Paul F, Arkin Y, Giladi A, *et al.* Transcriptional heterogeneity and lineage commitment in myeloid progenitors. *Cell* 2015;**163**(7): 1663–77.
147. Buettner F, Natarajan KN, Casale FP, *et al.* Computational analysis of cell-to-cell heterogeneity in single-cell RNA-sequencing data reveals hidden subpopulations of cells. *Nat Biotechnol* 2015;**33**(2):155–60.
148. Biase FH, Cao X, Zhong S. Cell fate inclination within 2-cell and 4-cell mouse embryos revealed by single-cell RNA sequencing. *Genome Res* 2014;**24**(11):1787–96.
149. Deng Q, Ramskold D, Reinius B, *et al.* Single-cell RNA-seq reveals dynamic, random monoallelic gene expression in mammalian cells. *Science* 2014;**343**(6167): 193–6.
150. Klein AM, Mazutis L, Akartuna I, *et al.* Droplet barcoding for single-cell transcriptomics applied to embryonic stem cells. *Cell* 2015;**161**(5):1187–201.
151. Goolam M, Scialdone A, Graham SJL, *et al.* Heterogeneity in Oct4 and Sox2 targets biases cell fate in 4-cell mouse embryos. *Cell* 2016;**165**(1):61–74.
152. Kim JK, Kolodziejczyk AA, Ilicic T, *et al.* Characterizing noise structure in single-cell RNA-seq distinguishes genuine from technical stochastic allelic expression. *Nat Commun* 2015;**6**:8687.
153. Usoskin D, Furlan A, Islam S, *et al.* Unbiased classification of sensory neuron types by large-scale single-cell RNA sequencing. *Nat Neurosci* 2015;**18**(1):145–53.
154. Zeisel A, Munoz-Manchado AB, Codeluppi S, *et al.* Brain structure. Cell types in the mouse cortex and hippocampus revealed by single-cell RNA-seq. *Science* 2015;**347**(6226): 1138–42.
155. Yu Z, Liao J, Chen Y, *et al.* Single-cell transcriptomic map of the human and mouse bladders. *J Am Soc Nephrol* 2019;**30**(11): 2159–76.
156. Tusi BK, Wolock SL, Weinreb C, *et al.* Population snapshots predict early haematopoietic and erythroid hierarchies. *Nature* 2018;**555**(7694):54–60.
157. Pijuan-Sala B, Griffiths JA, Guibentif C, *et al.* A single-cell molecular map of mouse gastrulation and early organogenesis. *Nature* 2019;**566**(7745):490–5.
158. Cao J, Spielmann M, Qiu X, *et al.* The single-cell transcriptional landscape of mammalian organogenesis. *Nature* 2019;**566**(7745):496–502.
159. Setty M, Tadmor MD, Reich-Zeliger S, *et al.* Wishbone identifies bifurcating developmental trajectories from single-cell data. *Nat Biotechnol* 2016;**34**(6):637–45.
160. Nestorowa S, Hamey FK, Pijuan Sala B, *et al.* A single-cell resolution map of mouse hematopoietic stem and progenitor cell differentiation. *Blood* 2016;**128**(8):e20–31.
161. Cao J, Packer JS, Ramani V, *et al.* Comprehensive single-cell transcriptional profiling of a multicellular organism. *Science* 2017;**357**(6352):661–7.
162. Strehland A, Ghosh J. Cluster ensembles—a knowledge reuse framework for combining multiple partitions. *J Mach Learn Res* 2002;**3**:583–617.
163. McDaid AF, Greene D, Hurley N. Normalized mutual information to evaluate overlapping community finding algorithms *arXiv preprint arXiv:11102515*. 2011.
164. MacKay DJ, Mac Kay DJ. *Information Theory, Inference and Learning Algorithms*. Cambridge University Press, 2003.
165. Hubert L, Arabie P. Comparing partitions. *J Classif* 1985;**2**(1): 193–218.
166. Buttner M, Miao Z, Wolf FA, *et al.* A test metric for assessing single-cell RNA-seq batch correction. *Nat Methods* 2019;**16**(1): 43–9.
167. Rosenberg A, Hirschberg J. V-measure: a conditional entropy-based external cluster evaluation measure. In: *Proceedings of the 2007 Joint Conference on Empirical Methods in Natural Language Processing and Computational Natural Language Learning (EMNLP-CoNLL)*, 2007. 410–20.